Insights into the Hydromechanical Behavior of a River Embankment through Physical and Numerical Modeling

Elena Dodaro, Ph.D.[1]; Daniela Giretti, Ph.D.[2]; Marianna Pirone, Ph.D.[3]; Roberta Ventini, Ph.D.[4]; Vincenzo Fioravante, Ph.D.[5]; Guido Gottardi, Ph.D.[6]; and Claudio Mancuso, Ph.D.[7]

Abstract: In the framework of a climate change scenario and growing land urbanization, a reliable assessment of river embankment safety conditions represents a key aspect to enhance the resilience of these critical infrastructures and support the development of design guidelines and flood risk reduction strategies. This paper aims at contributing to a deeper understanding of the effect of hydraulic loadings on the hydromechanical behavior of unsaturated river embankments through physical and numerical modeling. To fulfill this scope, two centrifuge tests were conducted on a small-scale physical model, representative for the tributary bank systems of the main river in Italy, the Po River. The model embankment featured a trapezoidal-shaped cross section and was made of a compacted silty sand mixture, overlying a homogeneous clayey silt foundation layer. A comprehensive laboratory investigation was carried out to estimate the geotechnical properties of both materials and the main outcomes are herein presented. To monitor the model response to the imposed hydraulic boundary conditions, the middle section of the embankment was extensively instrumented with miniaturized tensiometers, pore pressure transducers, and displacement sensors. Subsequently, a coupled flow–deformation finite-element (FE) model was set up to replicate the two centrifuge tests. Once validated, the numerical model was adopted to study the performance of an embankment under realistic flood scenarios as its hydraulic characteristics varied. The development of this numerical model made it possible to create a predictive tool for the assessment of the hydromechanical behavior of existing river embankments. **DOI: 10.1061/JGGEFK.GTENG-12633.**

Author keywords: Centrifuge test; Coupled numerical analyses; River embankment; Unsaturated soil; Transient flow.

Introduction

Floods are inherently natural and unpredictable occurrences; nonetheless, human activities have contributed to increase their frequency and exacerbated the consequences in terms of damage, repairing costs, and loss of lives. The preservation of territories from inundation requires extensive investigation on the conditions of thousands of kilometers of existing earth structures, initially naturally formed and then typically built according to empirical guidelines. In particular, river embankments are frequently designed by adopting the simplified assumption of stationary flow, in equilibrium with the maximum expected river level, often not fully understanding the crucial role of the soil partial saturation. This is probably due to the well-known difficulties in estimating both positive and negative pore water pressure (PWP) distributions and the contribution of suction to the shear strength. However, recent experiences on full-scale and small-scale physical models, as well as real-time in situ monitoring activities, have widely demonstrated that for these geotechnical works, the variation of water content related to soil–atmosphere interaction and water level fluctuation have a determinant role in the overall earthworks' stability (Orlandini et al. 2015; Calabresi et al. 2013; Caicedo and Thorel 2014; Gottardi et al. 2016; Rivera-Hernandez et al. 2019; Jafari et al. 2019; Gottardi et al. 2020; Gragnano et al. 2021). Thus, the traditional approach considering the steady-state flow in fully saturated embankments may lead to excessively conservative design solutions and, more importantly, provide erroneous conclusions on the effective safety margins toward possible failure mechanisms. This also applies in the case of rapid drawdown, which causes instantaneous and time dependent changes in pore pressure distribution on the riverside slope. Therefore, to successfully design and select cost-effective countermeasures against potential collapse, a reliable modeling of flood events and rapid drawdowns phenomena requires a correct estimation of the effective stresses along with the actual extent of the saturated zone. In this regard, geotechnical centrifuge tests prove to be a valuable tool for examining the

[1]Postdoctoral Researcher, Dept. of Civil, Chemical, Environmental and Materials Engineering, Univ. of Bologna, Viale del Risorgimento 2, Bologna 40136, Italy (corresponding author). ORCID: https://orcid.org/0000-0002-5552-5504. Email: elena.dodaro2@unibo.it

[2]Associate Professor, Dept. of Engineering and Applied Science, Univ. of Bergamo, Viale Marconi 5, Dalmine 24044, Italy. ORCID: https://orcid.org/0000-0003-4145-1388

[3]Associate Professor, Dept. of Civil, Building and Environmental Engineering, Univ. of Napoli Federico II, Via Claudio 21, Napoli 80125, Italy. ORCID: https://orcid.org/0000-0002-2834-6500

[4]Engineer, Ministry of Infrastructures and Transport, Technical Office for Dams, Via dei Greci, 48, Napoli 80133, Italy. ORCID: https://orcid.org/0000-0001-6635-3456

[5]Full Professor, Dept. of Engineering, Univ. of Ferrara, Via Giuseppe Saragat, 1, Ferrara 44124, Italy.

[6]Full Professor, Dept. of Civil, Chemical, Environmental and Materials Engineering, Univ. of Bologna, Viale del Risorgimento 2, Bologna 40136, Italy.

[7]Full Professor, Dept. of Civil, Building and Environmental Engineering, Univ. of Napoli Federico II, Via Claudio 21, Napoli 80125, Italy.

Note. This manuscript was submitted on January 5, 2024; approved on November 25, 2024; published online on May 22, 2025. Discussion period open until October 22, 2025; separate discussions must be submitted for individual papers. This paper is part of the ***Journal of Geotechnical and Geoenvironmental Engineering***, © ASCE, ISSN 1090-0241.

hydromechanical response of river embankments in critical scenarios, especially given the challenges of obtaining field data under extreme hydraulic conditions. The use of geotechnical centrifuges for modeling problems, which involve the partially saturated state of soils, is increasing (Higo et al. 2015; Vorster et al. 2017; Rotisciani et al. 2020) due to the advantages offered by the application of an enhanced gravitational field, which addresses the fundamental issue of in situ stress state replicability. In the last few decades, several researchers have contributed to the investigation of river embankment response to simulated high-water events and drawdowns. In 1979, a series of model embankments, subjected to a planned sequence of rapid perturbations, was tested using the beam centrifuge of the University of Cambridge, in order to understand the causes of the collapses that occurred to River Thames embankments (Padfield 1979). Later on, other researchers focused on centrifuge models to investigate the interaction of hydrostatic uplift forces with embankment models (Hird et al. 1978; Cargill and Ko 1983; Padfield and Schofield 1983; Van et al. 2005; Saran and Viswanadham 2018; Singh et al. 2019; Amabile et al. 2020). However, most of these investigations neglected the monitoring of suction distribution changes; in addition, there are still some uncertainties regarding the estimation of the hydraulic conductivity within unsaturated porous media, under an enhanced gravity field (Harvard and Corey 1964; Mitchell 1994; Theriault and Mitchell 1997; Singh and Gupta 2000; Singh and Kuriyan 2002). Considering the key role played by the partial saturation on the stability of river embankments, this work attempts to provide an insight into the hydromechanical behavior of river embankments by combining physical and numerical modeling. In particular, two centrifuge tests on a partially saturated silty sand model embankment were designed and carried out to investigate the variation of partial saturation conditions inside the embankment as induced by flooding. The hydraulic boundary conditions imposed during the tests aimed at replicating two scenarios: (1) a high-water event of even unrealistic long persistence, but able to reach steady-state flow conditions in the embankment; and (2) a sequence of hydrometric peaks and drawdowns of different intensity and duration, during which the embankment experienced transient seepage conditions. The 7.5-m-high prototype embankment, made of silty sand, compacted at the optimum water content and dry unit weight of the Proctor Standard test, was founded on a 5-m-thick fine-grained layer. The testing materials were selected to be representative for the riverbank systems of the Apennines tributaries of the Po River and were thoroughly tested at the laboratory scale for a detailed definition of their hydromechanical properties. The middle section of the model was extensively instrumented with pore pressure transducers embedded in the foundation, tensiometers in the embankment, and displacement and rotation transducers to inspect the hydromechanical response of the model.

Since the final aim of this research is to calibrate a predictive numerical tool for assessing the safety conditions of existing river embankments, the outcomes of the centrifuge tests were used to validate a numerical tool capable of performing reliable predictive seepage and stability analyses. The observed experimental response was numerically reproduced through fully coupled flow–deformation analyses, developed by means of the FE software PLAXIS 2D (Bentley Systems Incorporated 2020). The behavior of earth structures is inherently coupled from a hydromechanical perspective, as strongly supported by scientific literature (Fredlund and Rahardjo 1993; Blatz et al. 2006; Lu and Likos 2004; Farias and Cordão Neto 2010). In particular, numerous case studies and numerical models have confirmed the critical importance of coupled hydromechanical approaches in understanding and predicting the stability of river embankments (Moffat and Fannin 2011; Rinaldi et al. 2004; Zhang et al. 2019; Chen and Zhang 2023). These investigations clearly show that taking into account the interactions between hydraulic and mechanical processes is essential for accurately assessing river embankment performance, particularly under varying boundary conditions. Ignoring flow–deformation interaction in the design and maintenance of these structures can lead to unexpected and potentially disastrous failures. Therefore, it is essential to integrate coupled flow–deformation approaches into predictive models, as done in this case, and geotechnical engineering practices, to ensure the safety and reliability of river embankments.

Finally, to test the reliability of the numerical tool, validated against the experimental centrifuge benchmark, a realistic critical scenario was investigated. Note that this study exclusively focuses on the effects of high-water events on the response of river embankments, intentionally disregarding other factors such as animal burrowing or human-induced deterioration, which are known to increase the local vulnerability and, consequently, the risk of failure during critical events. Even daily and seasonal cycles of wetting and drying, exacerbated by the effects of climate change, are acknowledged to cause shrinkage and swelling in earth infrastructure, such as railway and highway embankments, earth dams, and river embankments, especially in those characterized by fine-grained slopes, as highlighted by Clarke and Smethurst (2010). Indeed, profound cracks may lead to changes in hydraulic conductivity and in the infiltration regime within the soil, with substantial variations in soil parameters occurring both seasonally and gradually over time (Stirling et al. 2021). However, if the embankment material is highly compacted and its permeability appropriately low, there is little penetration of the saturation line even during severe high-water events and the decrease/increase in suction is limited to a thin zone near the boundaries and, in some cases, in the shallow foundation. On the contrary, the embankment core remains substantially unsaturated, as highlighted by Calabresi et al. (2013).

Testing Materials

River embankments are typically built using locally available borrow materials having a low to very low coefficient of permeability, to prevent the infiltration of water within the earth structures. Silty sand materials overlaying finer subsoils are peculiar in the Po River basin of northern Italy; thus, in order to reproduce this peculiar stratigraphy, the soils selected for the construction of the physical models were a mixture of silty clayey sand (TS70-PON30) for the embankment and Pontida sandy clayey silt (PON) for the foundation layer. The TS70-PON30 mixture was formulated by mixing Ticino sand (TS) and PON in a 7:3 ratio by dry weight. TS is a well-known Italian sand subjected to intensive conventional and advanced laboratory tests (Fioravante 2000; Fioravante and Giretti 2016) while PON is a low plasticity kaolinitic sandy clayey silt from Italy (Hueckel and Baldi 1990; Hueckel 1992; Ventini et al. 2021). Physical and mechanical properties of the TS70-PON30 mixture and PON are reported in Table 1, while the grain-size distributions (Ventini et al. 2021) are shown in Fig. 1(a).

The Embankment Material: The Mixture TS70-PON30

To simulate the in situ compaction processes typically performed during the construction of earth dams and embankments, the small-scale models were prepared at the optimum dry unit weight of 20.55 kN/m^3 and water content of 8.75%, as determined using the Standard Proctor (SP) compaction method [ASTM D698-12 (ASTM 2021)]. These conditions are illustrated in Fig. 1(b), along with the saturation domains. Consolidated drained triaxial tests, carried out according to the ASTM D7181-20 (ASTM 2020),

J. Geotech. Geoenviron. Eng., 2025, 151(8): 04025075

Table 1. Average values of index and mechanical properties of the tested materials

Soil	$e_{\min}$	$e_{\max}$	G_s	D_{50} (mm)	U_c	LL (%)	PL (%)	PI (%)	φ'_{cv} (degrees)	C_c	C_s	c' (kPa)	φ'_p (degrees)
PON													
At $\sigma'_{zp} = 200$ kPa (Test 1)	—	—	2.744	0.015	—	23.62	13.13	10.49	32	0.128	0.016	5	33.5
At $\sigma'_{zp} = 800$ kPa (Test 2)	—	—	2.744	0.015	—	23.62	13.13	10.49	32	0.128	0.016	12	32.0
TS70-PON30	0.236	0.953	2.684	0.458	246.1	17.66	10.23	7.43	36	0.068	0.013	—	—
At the optimum proctor standard dry density												0	46.0

Note: $e_{\min}$ = minimum value of void ratio; $e_{\max}$ = maximum value of void ratio; G_s = specific soil density; D_{50} = particle size; U_c = uniformity coefficient; LL = liquid limit; PL = plastic limit; PI = plasticity index; σ'_{zp} = preconsolidation stress; φ'_p = friction angle at peak; φ'_{cv} = friction angle at critical state; c' = effective cohesion; Cc = compression index; and Cs = swelling index.

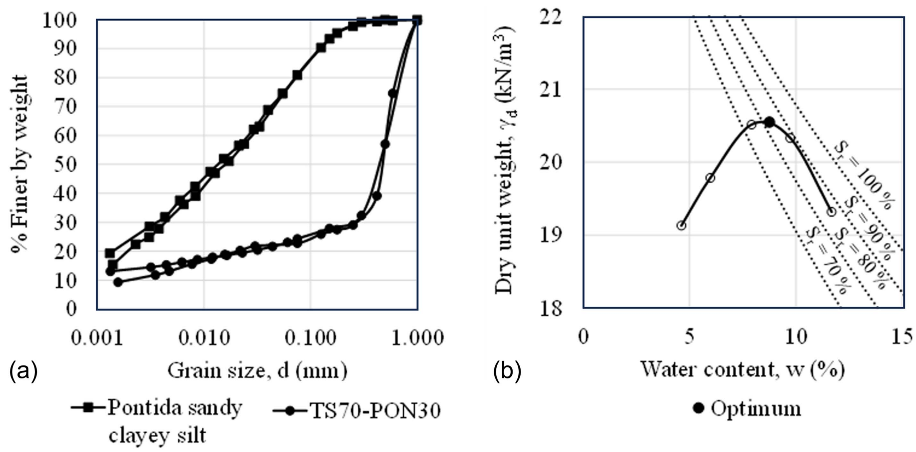

Fig. 1. (a) Grain-size distributions of the testing soils; and (b) standard proctor compaction curve for TS70-PON30 mixture.

were performed on three specimens of the TS70-PON30 mixture, compacted at the optimum SP and saturated by the application of a back pressure. The specimens were consolidated at the effective confining stresses of 50, 100, and 200 kPa, respectively, and sheared in compression, with drainage allowed, at a controlled rate of strain ($v = 0.05$ mm/min). Shear strength parameters at peak state are reported in Table 1. The mixture exhibited favorable mechanical properties in terms of the peak friction angle. In addition, the compressibility of the soil was investigated by means of standard oedometer tests on saturated specimens. Mean values of the compression index C_c and the swelling index C_s are reported in Table 1. The saturated hydraulic conductivity, k_{sat}, of the compacted mixture was obtained through constant head permeability tests, conducted in the triaxial apparatus [CEN ISO/TS 17892-11 (CEN ISO/TS 17892-11:2004 - UNI Ente Italiano di Normazione 2004)] on specimens taken from the Proctor mold, by imposing a low hydraulic gradient between the base and the top of each sample, obtaining an average value of 2.73×10^{-7} m/s. Then, the estimation of soil water retention curves (SWRCs) and hydraulic conductivity functions (HCFs) was performed by means of the standard HYPROP apparatus by METER (Schindler et al. 2010). The equipment hosts cylindrical samples measuring 50 mm in height and 80 mm in diameter and allows for the measurement of the pressure head at two different depths, through miniaturized tensiometers positioned at 12.5 and 37.5 mm from the base, while water evaporates from its surface. At the end of the experiment, the soil sample is dried at 105°C and weighted to calculate the oven-dry bulk density. Water loss is determined by continuously weighing the system, while volumetric water content at each time step, θ_i, is calculated by dividing the mass of the soil water by the total volume of the soil body and assigned to a tension that is determined from the average measurements of the two tensiometers. In order to estimate the HCFs, it was assumed that the water flow through a horizontal plane lying between the two tensiometer tips is

$$q_i = \frac{\Delta V_i}{\Delta t_i} \tag{1}$$

where ΔV_i is the change in water volume derived from the weight variation during the test and Δt_i is the time interval between two calculation time steps.

Then, data points for the hydraulic conductivity function are calculated by inverting Darcy's equation (Darcy 1856). To obtain the residual part of the SWRCs, the evaporation tests were coupled to high suction range psychrometric measurements, performed by means of the WP4C - Dew Point Potentiometer, by METER (Kirste et al. 2019). According to this method, suction is determined by equilibrating the sample in an enclosed chamber, through the dew point temperature and subsequently measuring the vapor pressure of the environment, in equilibrium with the sample. Raw data in terms of pressure heads, water contents, and evaporation fluxes have been interpolated by means of a Hermitian spline function, to obtain the SWRCs and the HCFs. The software HYPROP-FIT (Pertassek et al. 2015), which implements the simplified evaporation method, as outlined by Peters and Durner (2008), Schindler et al. (2010), and Schindler and Müller (2017), has been used to derive the trends of the aforementioned curves. The Mualem–van Genuchten MVG (Mualem 1976; Van Genuchten 1980) was selected as retention model to fit the experimental data, through the following relation:

Table 2. Saturated hydraulic conductivity coefficient k_{sat} and hydraulic parameters of the Mualem–van Genuchten (MVG) retention model (θ_r residual volumetric water content; θ_{sat} saturated volumetric water content; α_{VG}, n_{VG} and l fitting parameters) of the TS70-PON30 and the PON specimens

	k_{sat}	θ_r	θ_{sat}	α_{VG}	n_{VG}	l	AEV
Specimen	m/s	—	—	1/kPa	—	—	kPa
SP1	4.06×10^{-7}	0	0.225	0.117	1.233	−4.840	3.95
SP2	1.80×10^{-7}	0	0.216	0.057	1.241	−2.898	8.06
SP3	2.33×10^{-7}	0	0.206	0.067	1.236	−2.999	6.88
Average	2.73×10^{-7}	0	0.215	0.080	1.236	−3.579	6.29
PON1	7.70×10^{-9}	0	0.323	0.023	1.37	−0.29	19.04
PON2	4.13×10^{-10}	0	0.373	0.007	1.455	−0.584	60.71
Average	4.06×10^{-9}	0	0.348	0.015	1.413	−0.437	39.87

$$S_e(s) = \frac{\theta - \theta_r}{\theta_s - \theta_r} = \left[\frac{1}{1 + \left(\frac{s}{\alpha_{VG}}\right)^{n_{VG}}}\right]^{m_{VG}} \tag{2}$$

where S_e is the effective saturation degree; θ, θ_s, and θ_r are the current, saturated, and residual volumetric water content, respectively; and s is the matric suction. The parameter α_{VG} is related to the air entry value of the soil (AEV); n_{VG} is a shape factor, influenced by the rate of water extraction from the soil, affecting the steepness of the water retention curve; and m_{VG} is a dependent parameter that is typically calculated using Eq. (3) from Mualem (1976)

$$m_{VG} = 1 - \frac{1}{n_{VG}} \tag{3}$$

The relationship between the effective degree of saturation and the hydraulic conductivity, k, is expressed by Eq. (4)

$$k = k_{sat} \cdot S_e^l \cdot \left[1 - \left(1 - S_e^{\frac{1}{m_{VG}}}\right)^{m_{VG}}\right]^2 \tag{4}$$

where l affects the decrease in permeability with suction. AEVs were determined according to Wang et al. (1997), by using the following expression:

$$AEV = \frac{1}{\alpha_{VG}} m_{VG}^{\frac{1}{n_{VG}}} \tag{5}$$

The MVG model parameters estimated for both the TS70-PON30 and the PON specimens are reported in Table 2. The SWRCs and HCFs are shown along with the experimental data in Fig. 2.

The HCF obtained by using the mean MVG model parameters is also reported in Fig. 2. As expected, the TS70-PON30 mix representative of coarser textured soils loses water quickly as a direct reflection of the distribution and size of pores in the soil. The TS70-PON30 mix presents an air entry suction on average equal to 6.29 kPa, which is a typical value for sandy soils (Dias et al. 2022). Then, it is worth noting that the saturated hydraulic conductivity of the mixture is much higher if compared with that determined on PON due to the different grain-size distribution, as clearly visible in Fig. 2.

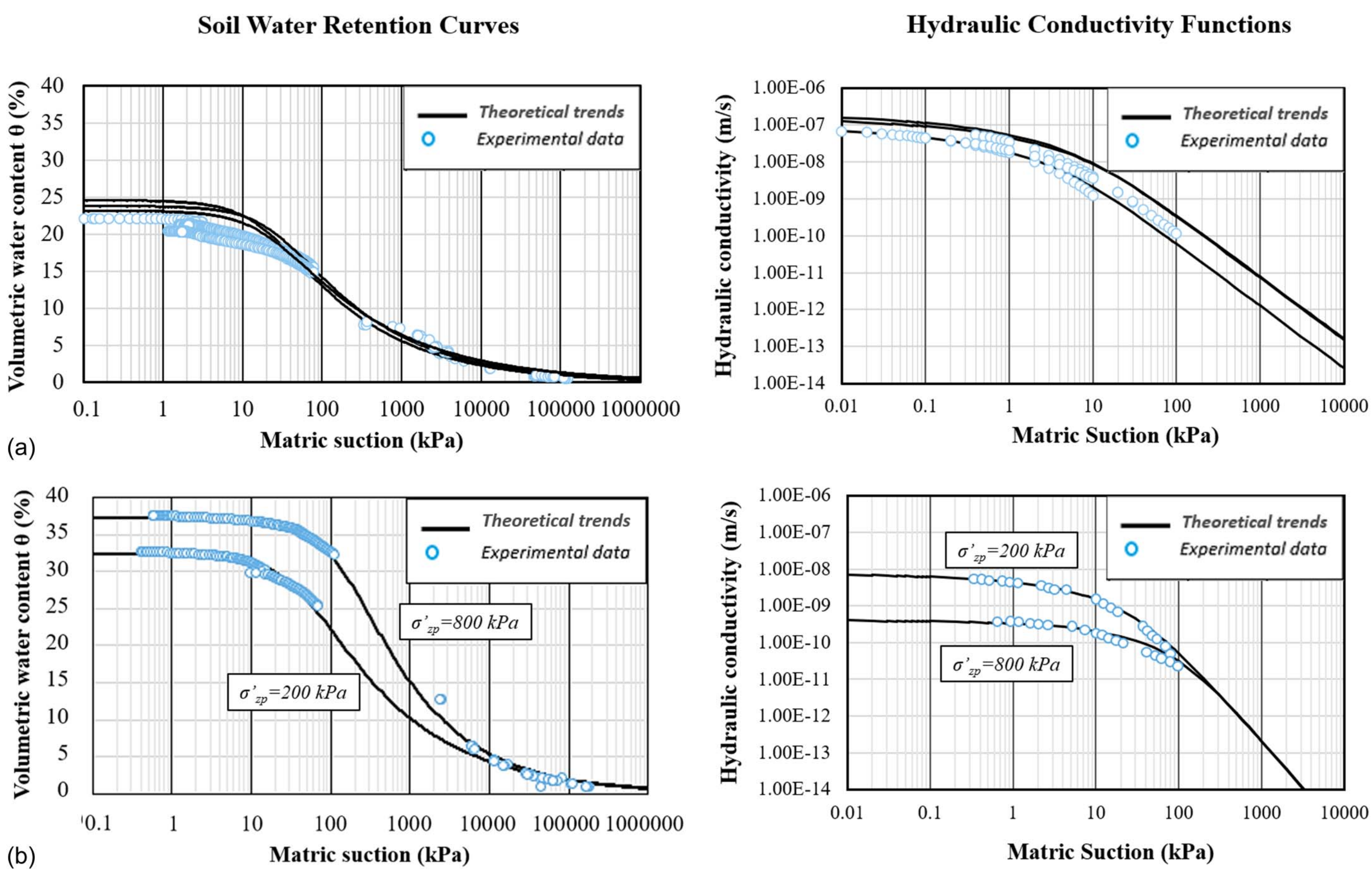

Fig. 2. Results of the evaporation tests and psychrometric measurements for: (a) TS70-PON30; and (b) PON specimens.

The Foundation Material: The Pontida Clay

In the two centrifuge tests carried out, the PON foundation layer had a different overconsolidation ratio, obtained by a $1g$ preconsolidation of a slurry at a vertical effective stress of 200 kPa (Test 1) and 800 kPa (Test 2). Three triaxial specimens from each sample were retrieved for consolidated drained tests at effective confining stress of 50, 100, and 200 kPa for a preconsolidation stress $\sigma'_{zp} = 200$ kPa and 50, 100 and 150 kPa for $\sigma'_{zp} = 800$ kPa. The specimens were saturated by the application of a back pressure, consolidated, and then sheared in compression, with drainage allowed, at a controlled rate ($v = 0.015$ mm/min). Shear strength parameters at peak state are reported in Table 1, together with the compressibility indexes. The shear strength at the peak state is similar in terms of friction angle, regardless of the preconsolidation stress. The average permeability of PON was indirectly derived from standard oedometer tests, as a function of the primary consolidation and compressibility coefficients, according to Terzaghi's one-dimensional consolidation theory. The hydraulic saturated conductivity thus determined results two orders of magnitude lower than that of the mixture adopted for the body of the river embankment (Table 2). The aforementioned same test procedure for the mixture was applied to investigate the SWRCs of PON for the two different preconsolidation stresses. Results are reported in Table 2 and Fig. 2, as discussed in the previous section. The PON presents an air entry suction on average equal to 40 kPa, which is a typical value for silty clay materials.

Centrifuge Modeling

Geometry and Instrumentation Layout

The tests were run using the 6 m diameter seismic centrifuge at the ISMGEO laboratory in Italy (Baldi et al. 1988; Airoldi et al. 2016). The geometrical scaling factor was $N = 50$ and the acceleration of $50g$ was applied at the model base. The embankment was 150 mm high (7.5 m at the prototype scale) with a riverside and landside slope of 1V:1H and 1.5V:1H, respectively. This design choice aimed to promote potential instability of the landside slope and, in any case, to observe a significant variation in the safety factor, in relation to changes in hydraulic boundary conditions imposed, in order to bring the earth structure to a condition of incipient collapse. Crest and base were 60 mm and 310 mm wide, respectively (3 m and 15.5 m at the prototype scale). The embankment was founded on a 100-mm-deep fine-grained layer (5 m at the prototype scale). Details of the geometry and sensor layout of the tests are given in Fig. 3(a). The models were reconstituted within a prismatic strongbox, 620 mm long, 445 mm high, 160 mm wide and were laterally visible through a thick acrylic glass window, as shown in Fig. 3(b). As highlighted in Fig. 3(a), eight miniaturized tensiometers, TENS (2–10), able to measure both positive and negative pressures up to ± 500 kPa, were embedded in the model embankment to monitor the evolution of suction as a function of time and hydraulic loading. Two linear displacement transducers (LDTs) (L1 and L3) monitored the vertical settlement of the crest; two rototranslative sensors (LR2 and LR5) measured the landside slope displacements. Four pore pressure transducers (PPTs) (N, P, Q, R) were located in the foundation layer; two further PPTs measured the water level riverside (M) and landside (255). Sensors were located along the vertical midsection of the model. Target markers were embedded in the lateral section of the embankment exposed by the transparent window for digital image analysis.

Two tests were performed, referred to as 1 and 2 from now on. These differ in terms of geometry as follows:

1. In the position of PPT M, located at the base of the embankment in Test 1 [M' in Fig. 3(a)] and at the base of the container, within a sandy well drilled in the foundation layer, in model 2 [M'' in Fig. 3(a)];
2. In the initial water head, which was zero in Test 1 and equal to 30 mm (1.5 m at prototype scale) in Test 2.

As aforementioned, the tests also differed for the $1g$ preconsolidation stress applied to the foundation layer and for the different loading history applied.

Model Reconstruction

The PON foundation layer was trimmed to the target thickness of 100 mm from a large sample preconsolidated in a consolidometer and moved within the test container. Then, the strongbox was filled for further 150 mm with the testing mixture compacted at the optimum water content and dry unit weight of the SP test. During the compaction of the soil layers, the tensiometers were positioned at the target locations. Finally, the embankment was shaped to the test geometry. PPTs were located in the foundation layer through horizontal drills realized from outside the back steel wall of the container and the drills were filled with a PON slurry.

Test Phases

The two tests were characterized by different hydraulic loading histories: the first river embankment model was subjected to steady-state seepage conditions, while in the second test, a sequence of hydrometric peaks and drawdown were imposed, to investigate the response of the embankment to transient groundwater flow.

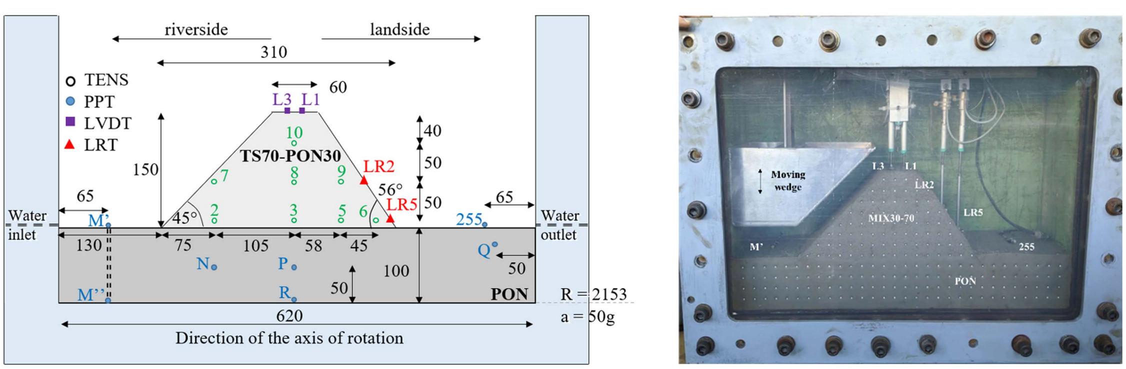

(a) (b)

Fig. 3. (a) Scheme of the model embankment tested in centrifuge (length unit in mm); and (b) picture of the model at the end of the reconstruction.

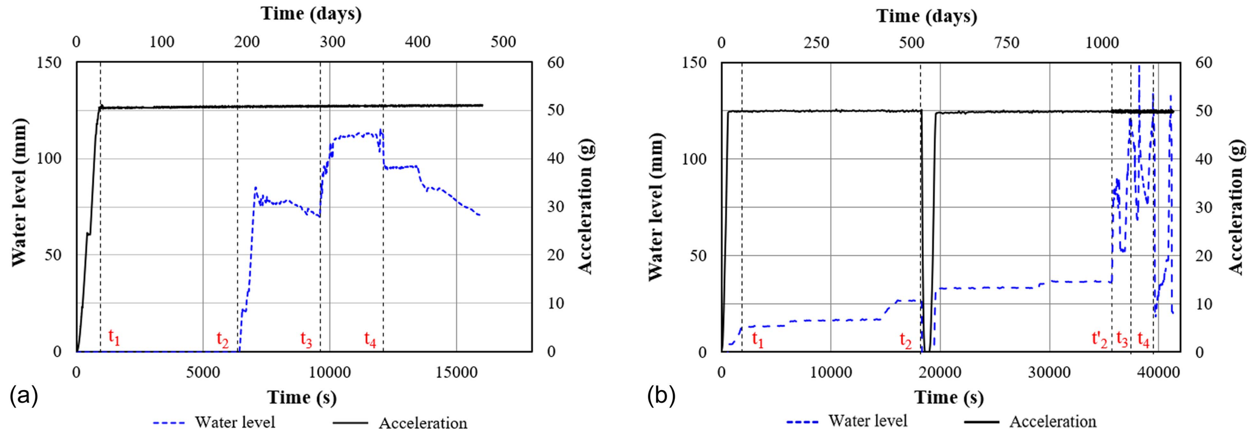

Fig. 4. Time history of hydraulic loadings: (a) Test 1; and (b) Test 2.

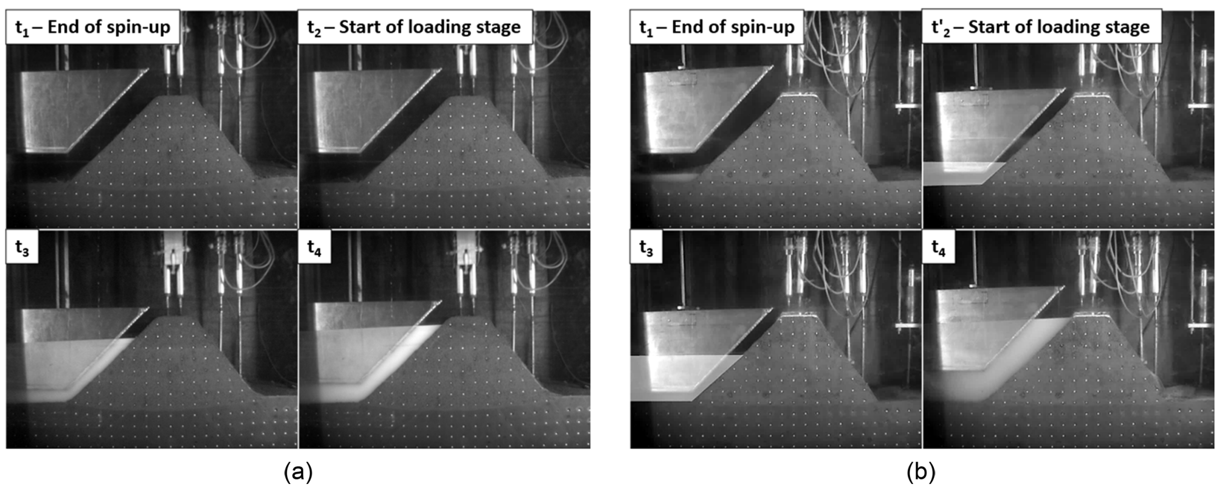

Fig. 5. Pictures of the models at relevant time instants: (a) Test 1; and (b) Test 2.

As shown in Fig. 4, where the hydraulic boundary condition applied during the tests is plotted together with the centrifuge acceleration, the tests were designed in phases: application of acceleration to target angular velocity, achieving in flight self-weight equilibrium, and application of hydraulic loadings. The testing fluid, consisting of water blended with a white pigment to enhance visibility, was stored in an external tank connected to the model via a controllable valve-equipped pipe. Monitoring of the riverside water level was accomplished via PPT M, as depicted in Fig. 4(a). When a specific level was attained, the valve was promptly closed, and subsequent regulation of the river level was achieved through a hydraulic actioned wedge, depicted in Figs. 3(b) and 5.

Test 1

The model was accelerated to the target angular velocity (from time 0 to time t_1) and allowed to approach the self-weight equilibrium (from t_1 to t_2). The initial water head was zero [Figs. 4(a) and 5(a)]. The centrifuge spin-up caused progressive settlement of the model, as visible in Fig. 5(a), mainly due to the deformation of the foundation layer under the footprint of the embankment. At t_2 [Figs. 4(a) and 5(a)], the consolidation settlement rate was considered sufficiently low and the hydraulic loading was then applied. The river rising was executed in two steps: first, up to a level equal to 60% of the embankment height [Fig. 5(a)]. This level was kept constant up to t_3 (approximately 60 days at the prototype scale). Then, the river was elevated to 82% of the embankment height and held constant for a further 46 days. After t_4, the level was lowered. The applied loading sequence does not represent a realistic flood event, since it is characterized by an unrealistic duration of the hydrometric peaks, intentionally maintained until a steady-state seepage condition was achieved in the embankment, with the aim of observing the evolution of the hydraulic characteristics within the earthworks and validating the hydromechanical characterization.

Test 2

The model was accelerated to the same angular velocity as in Test 1 and allowed to approach the self-weight equilibrium up to t_2 [Fig. 4(b)]. Water was provided to the riverside from the beginning of the test and progressively adjusted to reach a head of about 30 mm before the loading stage, to compensate for the loss of water due to seepage. In this test, a longer consolidation time was used [see Fig. 4(b)] in order to get closer to the equilibrium pore pressure distribution in the foundation layer. A technical issue to the wedge actuator required the centrifuge to be stopped and reaccelerated, so a second consolidation, of almost the same duration, was carried out up to t_2' [see Fig. 4(b)], with a total duration of about 520 days, against the 185 days of Test 1. The second model was subjected to a sequence of hydrometric peaks and drawdowns, representative of subsequent flood events, with a total duration of 160 days and characterized by rising and lowering of the variable rate. The applied water level ranged from 60% [time t_3 in Figs. 4(b) and 5(b)] to 95% (time t_4) the embankment height. A fast overtopping event, caused by a miscontrol of the wedge, occurred in correspondence of the third hydrometric peak. It is worth noting that (1) the applied loading sequence is representative of a possible sequence of high-water events, not necessarily realistic but meant to investigate the response of the embankment to transient seepage; and (2) the target hydrograph was quite regular, while limitations in the functioning of the actuator actioning the wedge resulted in an extremely variable loading history.

Test Results

In this section, the outcomes of the two centrifuge tests, in terms of vertical and horizontal displacements, as well as positive and negative PWPs recorded during all the stages of the experiments, are presented and discussed.

Test 1

The trend of displacements versus time recorded by the LDTs (L1 and L3) and rototranslative (LR2–LR5) sensors during all the stages of Test 1 is reported in Fig. 6(a). Vertical displacements Y are positive if downward; horizontal displacements X are positive if landward. It is noticeable that the greater part of the vertical displacement occurred as a result of the increment of the angular speed of the centrifuge to the target, while minor displacements can be observed during the in-flight consolidation stage and even smaller ones throughout the simulated flood event. The total settlement of the embankment crest, equal to 8.0 mm at the end of the flood event, slightly tends to increase also during the last stage of the test, in which the water level is gradually lowered. The rototranslative sensors LR2 and LR5 show a modest increase in the displacements toward the landside; conversely, the toe of the riverside slope moved in the opposite direction, as deduced from the captured images. This combined displacement has contributed to reduce the inclination of the slopes, bringing the embankment to a more stable configuration. Steady conditions were reached without the occurrence of any failure mechanism, both on the landside and riverside. Nevertheless, it is widely acknowledged that structural failure often necessitates a combination of triggering factors, such as a high-water event, along with wetting of the earthfill due to antecedent atmospheric events, such as precipitations, spring snow melting, and/or the presence of local weaknesses or cavities caused by animals burrowing or anthropic activities (Palladino et al. 2020; Saghaee et al. 2017), all disregarded in this study.

The left chart in Fig. 7(a) reports the time history of PWPs, measured during Test 1, by the eight miniaturized tensiometers installed in the embankment body; the right chart is a zoom on the flooding phase. All these sensors registered an initial mean suction of about 5 kPa, which progressively tends to increase, especially in the upper part of the embankment, during the spin-up of the model and the subsequent self-weight equilibrium stage. This occurred because model surfaces were exposed to the internal temperature of the shell, which covers and rotates together with the centrifuge arm, thus favoring evapotranspiration processes.

The sensors installed in the lower part of the embankment waterside (7, 2) instantaneously reflect the hydraulic level rising, as hydraulic conductivity was likely close to the value at saturation before the application of hydraulic load. Instead, tensiometers 9 and 10 were crossed by phreatic line only in correspondence of the second hydraulic peak. Excess PWPs were generated in the fine-grained foundation layer [as shown in Fig. 8(a)] during the spin-up of the model, then, once the target acceleration of $50g$ was reached, PWP started to decrease toward the hydrostatic distribution (equilibrium condition). The effect of a water level increase on the foundation layer is a further development of excess PWP, which dissipated during the constant load stages.

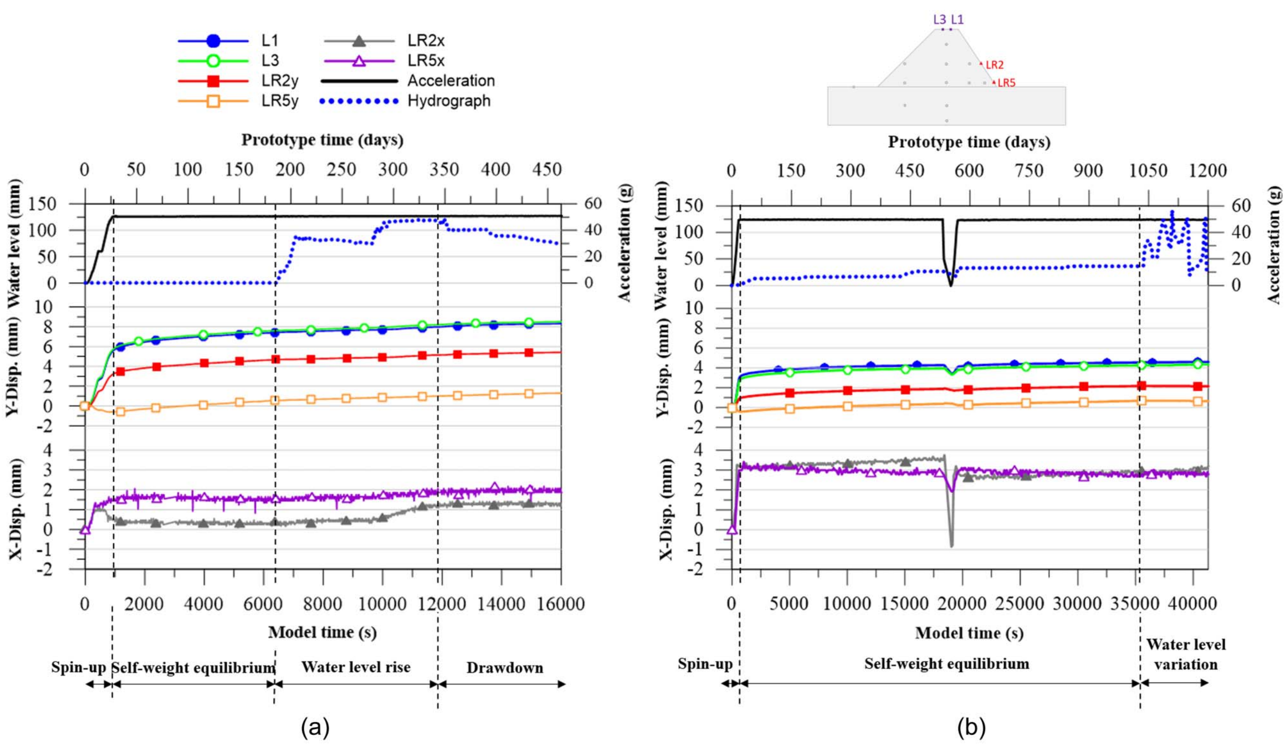

Fig. 6. Vertical and horizontal displacements recorded by LDTs and rototranslative sensors in: (a) Test 1; and (b) Test 2 at the model scale.

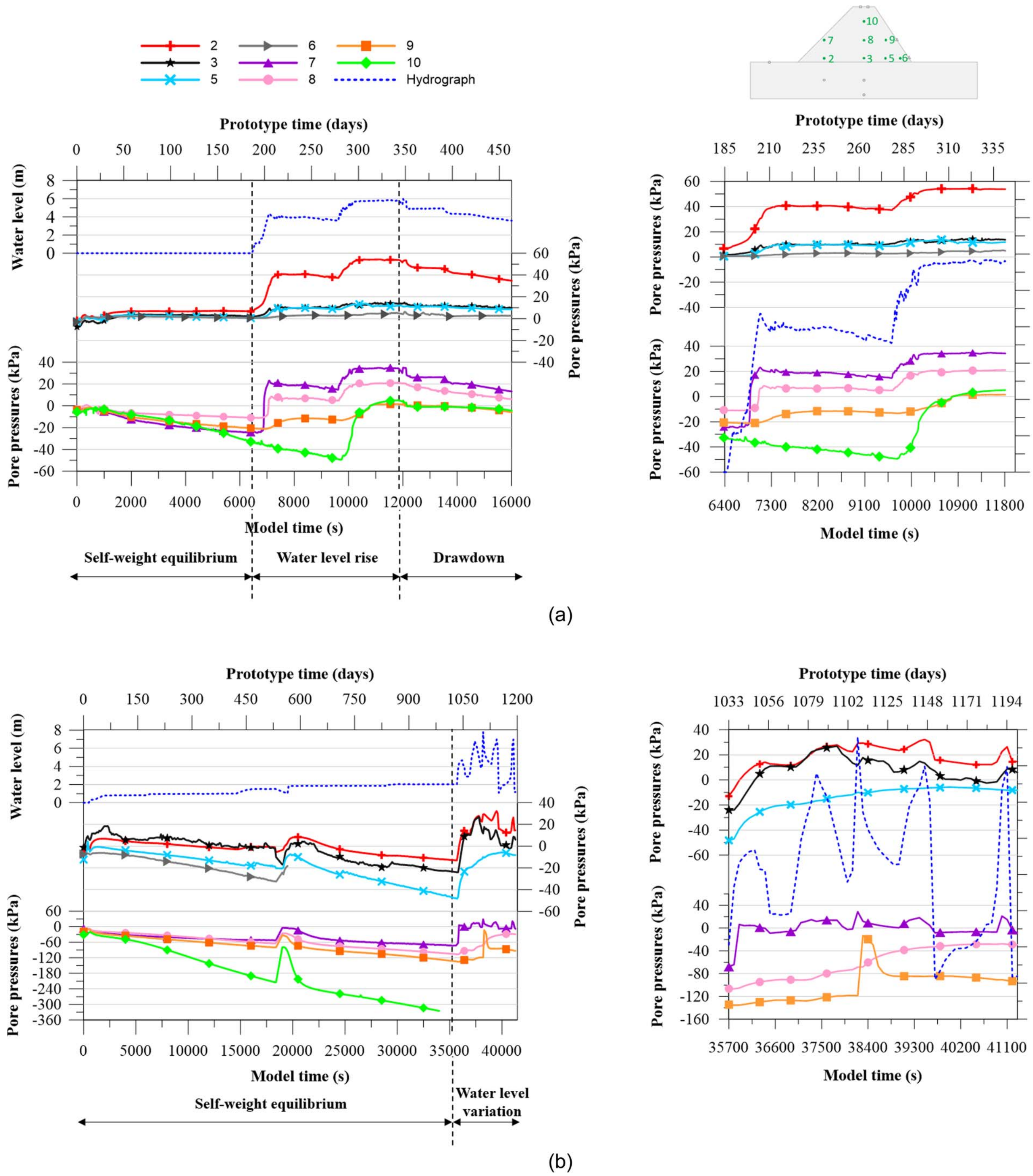

Fig. 7. PWPs recorded by tensiometers embedded in the embankment body, during: (a) Test 1; and (b) Test 2. Left charts: time history of pore pressure along the whole test; right charts: zoom on the flooding phase.

For further details of the hydraulic regime occurring in the model, isochrones of PWP along two verticals (crossing the sensors 7, 2, and N, and 10, 8, 3, P, and R) and two horizontal sections (crossing the tensiometers 7, 8, and 9 and 2, 3, 5, and 6) are plotted in Fig. 9. By looking at the vertical profiles in Figs. 9(a and b), at the beginning of the loading phase ($t_2 = 6{,}370$ s) suction distribution in the embankment got close to hydrostatic conditions while the foundation layer was still consolidating, with water flow directed both upward (from P to 3) and downward (from P to R). At the same time (t_2), a water flow directed horizontally from waterside to landside established at the bottom of embankment [Figs. 9(c and d)]. From the first to the second peak level ($t_3 = 7{,}130$ s to $t_4 = 10{,}380$ s), the crest of the levee progressively saturated [Fig. 9(b)] and a horizontal groundwater flow, characterized by very high gradients, developed within the embankment body [see Figs. 9(c and d)]. At the same time, the consolidation process started in the previous phase continued in the foundation layer with the water flow vertically directed toward the embankment and the bottom of the box.

It should be noted that the container walls were internally coated with Teflon and smeared with silicon grease before the model reconstruction, to waterproof the interface between the soil and

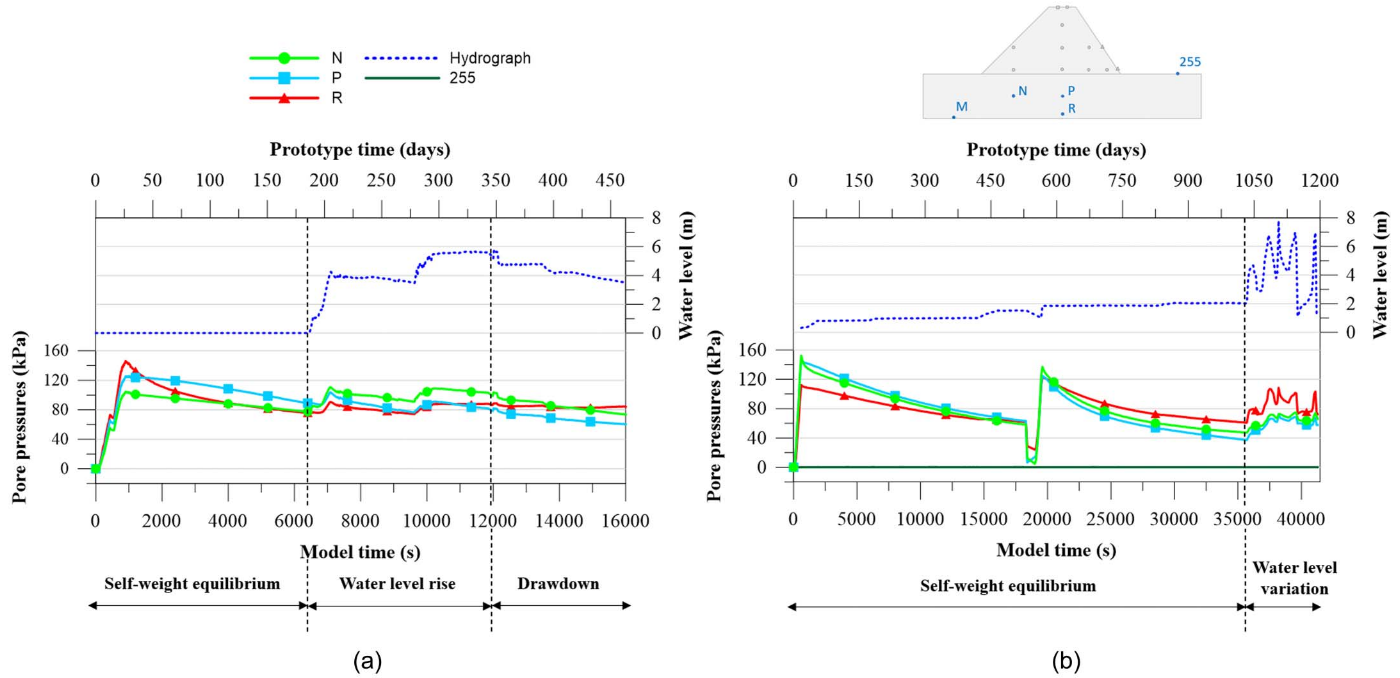

Fig. 8. PWPs recorded by PPT sensors located in the foundation and the lower part of the embankment during: (a) Test 1; and (b) Test 2.

the steel, while the container bottom is a draining surface, due to the presence of grooves. The observed downward dissipation indicates the establishment of a drainage path from the middle of the foundation layer toward the bottom and then upward along the walls, likely due inadequate waterproofing. However, this phenomenon did not influence the response of the embankment to the flooding.

Summing up, these results prove that the embankment under investigation reaches steady conditions only after an unrealistic persistence of the water level riverside, remaining in partially saturated conditions for a long time (Ventini et al. 2023). Therefore, the performance of the embankment under realistic hydraulic boundary conditions must undoubtedly be analyzed within the framework of unsaturated soil mechanics.

Test 2

The trend of displacements versus time recorded by the LDTs and rototranslative sensors during all the stages of Test 2 is reported in Fig. 6(b). Similarly to Test 1, the greater vertical displacement, as measured by LDTs located at the embankment crest, occurs during the first stage of the experiment. This phenomenon coincides with the acceleration of the centrifuge to $50g$. Minor settlements occur during the self-weight equilibrium phase, and even smaller displacements are observed throughout the following stages, which involve wetting–drying cycles. It can be noticed that the increase in the preconsolidation stress of the PON layer with respect to Test 1 (800 kPa versus 200 kPa) leads to a halving of the total settlement, equal to about 4 mm at the end of the test. On the contrary, the rototranslative sensors LR2 and LR5, located on the landside slope, exhibited larger horizontal displacements compared to Test 1. This included a sudden increase in the displacements toward the landside during the spin-up stage, probably related to the filtration flow directed horizontally from waterside to landside, due to the small head imposed waterside from the beginning of the test. The displacement increase is followed by a stable trend throughout the observation period, confirming the steadiness of the embankment, even after repeated water level changes. Despite the very rapid drawdowns applied, even in this test, the embankment resulted stable [Fig. 6(b)].

The evolution of PWPs over time, measured during the whole of Test 2, by the miniaturized tensiometers embedded in the embankment body is plotted in Fig. 7(b). The initial mean suction value of 5 kPa, measured above the water table, confirms the homogeneity of the soil used for the reconstruction of the models. The main difference with respect to the first test relies in the suction distribution attained before the imposition of the time-dependent hydraulic boundary conditions, due to a longer consolidation. This caused a desaturation due to evapotranspiration of the embankment higher than planned, with suction values of more than 300 kPa recorded in the upper part of the earth structure, at the end of the consolidation stage. Tensiometer 10 cavitated before the imposing of the variable hydraulic loading, probably due to the excessive drying of its high-air-entry-value porous stone. Tensiometer 6 ceased to work during the centrifuge stop.

When the hydraulic loadings were applied at t_2', the tensiometers located in the proximity of the riverside (2 and 7) suddenly reflected the water level changes, quickly shifting to positive PWPs. The middle vertical instrumented line, tensiometer 3, already close to saturation, showed to be quite responsive to water level changes. Tensiometer 8 proved that the surrounding soil remained in unsaturated conditions during all the stages of the test; in fact, it recorded only a slight increase in the degree of saturation, related to the progressive advancement of the phreatic line during the succession of the hydrometric peaks. Moving toward the landside slope, tensiometer 5 recorded a progressive increase in the degree of saturation but did not reach positive PWPs, confirming that the phreatic line did not overcome the first half of the embankment. The suction values registered by tensiometer 9 remained significantly below the saturation threshold, excluding the time step subsequent to the overtopping that occurred in correspondence of the third hydrometric peak, during which an isolated and sudden increase in the PWP could be observed, probably ascribable to the presence of the overflown fluid on the landside slope.

Excess PWPs were generated in the fine-grained foundation layer [as shown in Fig. 8(b)] during the two spin-ups of the model, then, once the target acceleration of $50g$ was reached, PWP started

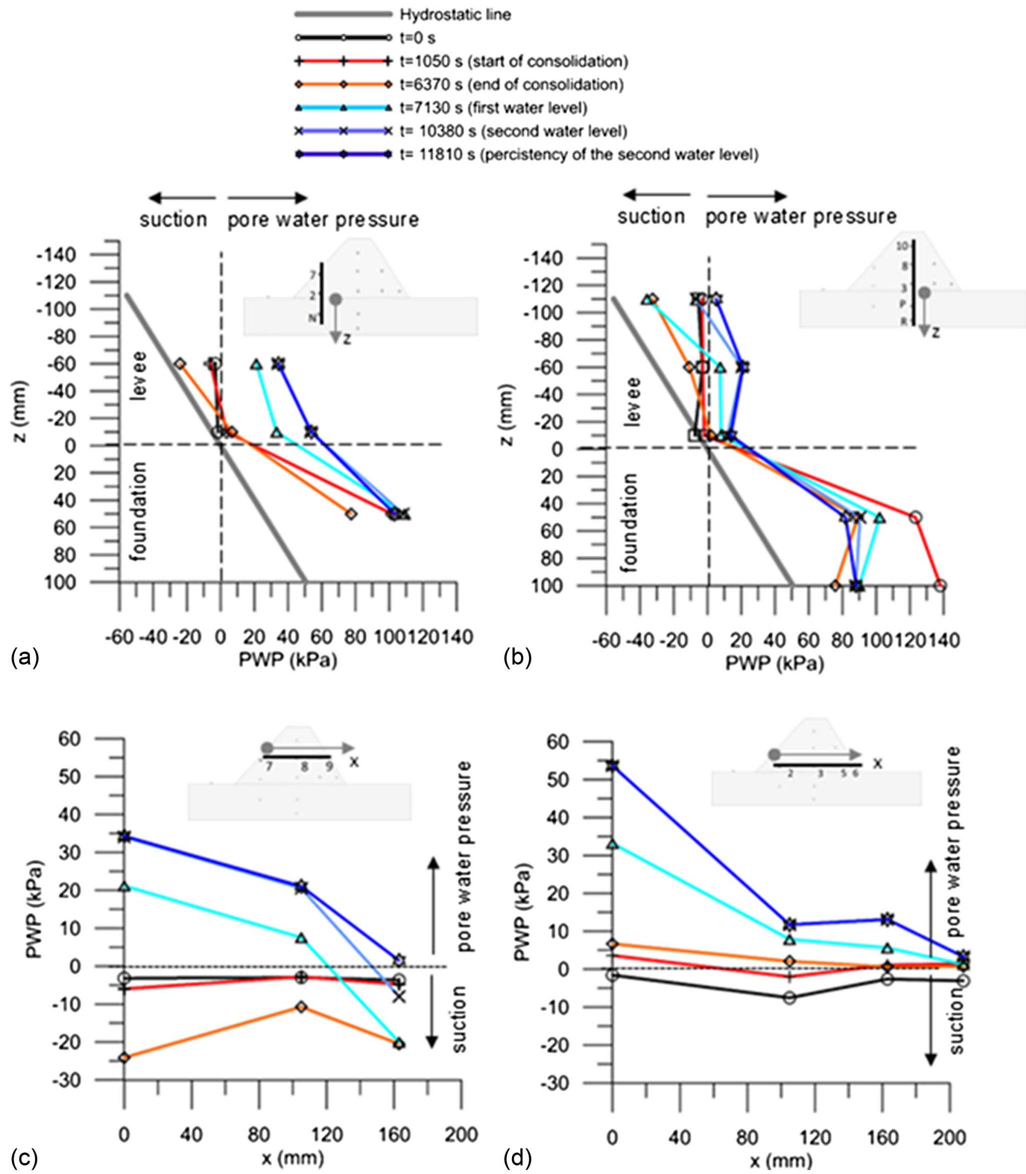

Fig. 9. Isochrones of PWPs at significant time-steps during Test 1: (a) vertical alignment 7-2-N; (b) vertical alignment 10-8-3-P-R; (c) horizontal alignment 7-8-9; and (d) horizontal alignment 2-3-5-6. The origin of the x-axis in plot (c and d) is located at the position of TENS 7 and TENS 2, respectively.

to decrease, getting closer to the hydrostatic distribution than the previous test, thanks to the longer consolidation stage. All the PPTs faithfully reproduce the hydraulic loading history imposed after t_2'. Isochrones of PWP are plotted in Fig. 10, along the vertical alignment 10, 8, 3, P, and R, and at the horizontal alignment 7, 8, and 9. By looking at the vertical profile at the end of consolidation [$t = 35{,}600$ s in Fig. 10(a)], suction distribution in the embankment results more than hydrostatic with water flow directed upward, while the consolidation process in the foundation layer is almost completed. At the same time, water flow at partially saturated conditions directed horizontally from waterside to landside establishes at the middle of embankment [Fig. 10(d)], due to the initial water head present on the riverside. The effects of the first peak inside the embankment ($t = 36{,}000$ s) are delayed; in fact, a decrease in suction with the achievement of positive PWPs at tensiometer 3 is observed at the first drawdown ($t = 36{,}830$ s) [Figs. 10(a and d)]. The second peak ($t = 37{,}450$ s) again produces a delayed small decrease in suction at the middle of embankment [at $t = 38{,}062$ s in Figs. 10(b and e)]; only the third peak, the highest one [$t = 38{,}200$ s in Figs. 10(b and e)], causes a variation of suction from 60 to 30 kPa at tensiometer 8.

Finally, the persistence of the fourth and the fifth peaks is very short, resulting in minimal impact on the matric suction within the embankment [Figs. 10(c and f)]. Under this hydrograph, a significant portion of the embankment remains partially saturated; the more the suction decreases, the faster the embankment responds to water level variation riverside, proving the key role played by suction on the hydraulic response of the embankments.

Finite-Element Numerical Modeling

In this section, back-analyses of the two centrifuge tests, carried out by using the FE code, PLAXIS 2D, by considering the full-scale prototype geometry, are presented. To validate the FE modeling, the results of the numerical simulations were compared with the outcomes of the centrifuge tests, which constitute a robust experimental benchmark. Finally, to assess the impact of proper hydraulic

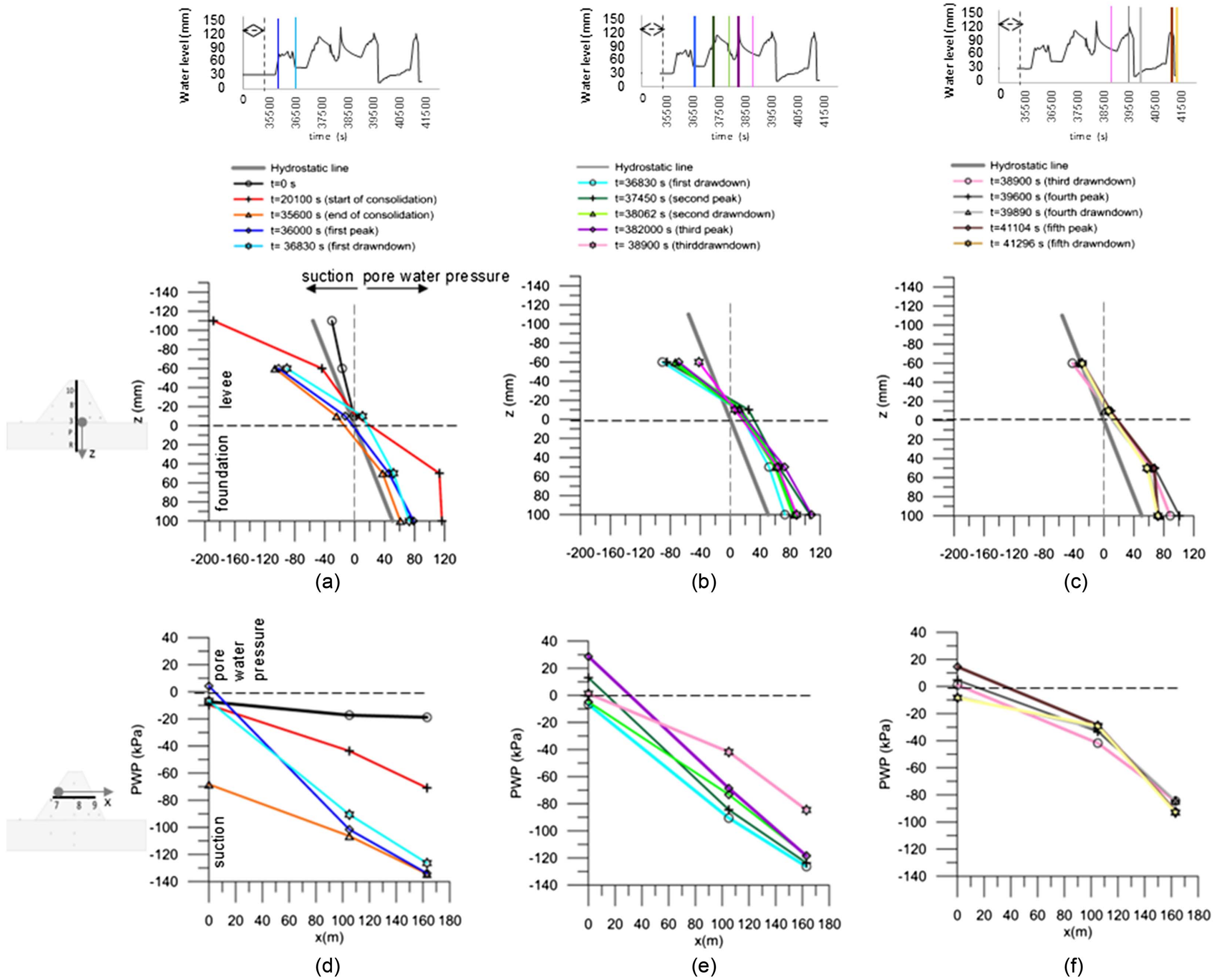

Fig. 10. Isochrones of PWPs at significant time-steps during Test 2: (a–c) vertical alignment 10-8-3-P-R; and (d–f) horizontal alignment 7-8-9. The origin of the x-axis in plot (d–f) is located at the position of TENS 7.

modeling, the numerical tool so calibrated was tested under a realistic flood scenario by varying the hydraulic properties of the earthfill. To accurately analyze the hydromechanical behavior of the tested soils by means of finite numerical methods, a coupled hydromechanical approach has been adopted. The effective stresses are computed by the code with the Bishop's approach (Bishop 1959) to account for partial saturation

$$\sigma' = (\sigma - u_a) + \chi(u_a - u_w) \tag{6}$$

where σ is the total stresses; σ' is the effective stresses; u_w and u_a are the PWP and the pore air pressure, respectively; and χ is an effective stress parameter, which varies from 0 to 1, covering the range from dry to fully saturated conditions. In PLAXIS, u_a is the atmospheric pressure and it is assumed to be 0, while χ is equal to the effective degree of saturation, S_{eff}.

The constitutive models adopted here, as subsequently specified, are able to capture the increase in soil shear strength due to the increase in suction, but they cannot simulate either the volumetric collapse nor the variation of the slope of the normal (λ) and unloading–reloading (κ) lines as suction changes.

Geometry, Mesh, and Material Properties

The geometry of the prototype utilized in the FE simulation was obtained by applying a scaling factor $N = 46.5$. This value corresponds to the centrifugal acceleration estimated at approximately half the height of the embankment ($z = 75$ mm from the crest), when considering the variation of the acceleration field as a function of the distance from the central axis of rotation. Fig. 11 reports a sketch of the plane strain section analyzed, including the adopted mesh and the position of nodes and stress points used for the comparison of numerical outcomes with the centrifuge monitoring data. The model geometry has been discretized with 2121 fifteen-node triangular elements, with an average size of 0.42 m. The mesh density underwent iterative optimization until no significant changes in PWP distribution were observed after refinement.

The Hardening Soil (HS) model, developed by Duncan and Chang (1970) under the framework of the plasticity theory, was adopted for modeling the mechanical behavior of the mixture. For the foundation layer, the Modified Cam-Clay (MCC) constitutive law, an elastic-plastic strain hardening model, based on critical state theory and proposed by Muir Wood and Graham (1990), was

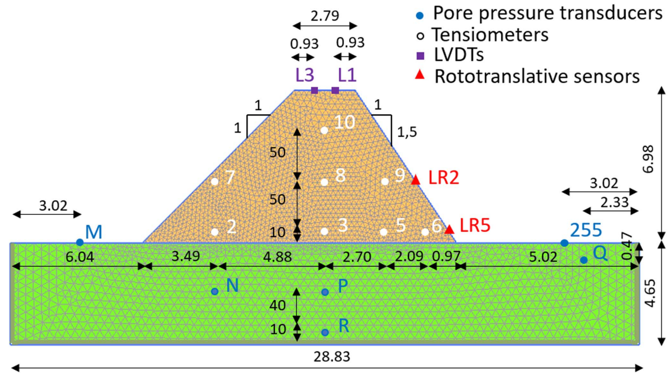

Fig. 11. Geometry of the plane strain section numerically analyzed; adopted mesh and instruments layout (length unit in m).

considered. Soil strength and stiffness parameters, calibrated based on the laboratory tests already described in this paper and assumed as input in the FE analyses, are listed in Table 3. Regarding hydraulic and retention properties of the mixture and the clayey silt materials, the non-hysteretic Mualem–van Genuchten model (Van Genuchten 1980) was adopted for the fitting of the experimental data, and the mean parameters reported in Table 2 were considered. The partial saturation of the embankment is modeled by the code adopting Eq. (6) for the calculation of the effective stresses. Therefore, the model is able to incorporate the influence of suction on soil shear strength. Nevertheless, the dependence of compression index, C_c, with suction and the phenomena of collapse on wetting that distinguish the compressible behavior of unsaturated soils, were neglected as HS was adopted as the constitutive model.

Calculation Phases

The peculiar conditions imposed by the centrifugal environment were properly accounted for in numerical analyses. To reproduce the construction stages of the model at $1g$, in the initial phase of the simulation, only the foundation layer was activated, and a pre-overburden pressure (POP) distribution, starting from the maximum stress values imposed at the ground level (i.e., 200 kPa for Test 1 or 800 kPa at Test 2) and linearly variable with depth, was considered to generate the preconsolidation stress of the soil strata. Vertical and horizontal effective stress-fields were initialized with the *K0 procedure*, a special calculation method available in PLAXIS 2D to define the initial stresses for the model, taking into account the loading history of the soil. Since the model was contained in a rigid steel box, the bottom horizontal, right, and left vertical sides of the foundation layer were assumed to be impermeable. As far as it concerns model constraints, a full fixity (a rough rigid boundary) was applied along the bottom of the model, while the vertical boundaries were fixed in the horizontal direction (smooth rigid boundary). In the second phase, the embankment construction was reproduced by means of an elastic-plastic deformation analysis (*Plastic analysis* in PLAXIS 2D) in which the foundation was assumed as fully saturated. A constant matric suction value of approximately 5 kPa was imposed in the embankment body while the water table was positioned at the ground level for Test 1 and at a height of 1.4 m riverside for Test 2, respectively. Then, the third phase consisted of a fully coupled flow–deformation analysis, finalized to replicate the suction distribution attained at the beginning of the flooding stage, due to the evapotranspiration occurring during the in-flight consolidation. Thus, negative PWP heads were imposed to the edges of the embankment and to the upper foundation boundaries. Nevertheless, the dissipation process of excess PWPs, developed in the foundation layer after the enhancement of the gravitational field, was neglected and a hydrostatic PWP distribution was assumed in the base layer, for both the analyses associated to Test 1 and 2. Finally, an additional fully coupled flow–deformation calculation was carried out to investigate the transient groundwater seepage flow due to the rising of the water level. In particular, a variable hydrometric condition, derived from PPT M measurements, was imposed on the riverside slope face, during the last stage of the analyses, to reproduce river level fluctuations in terms of total head above time, duly scaled according to the fluid diffusion law [Garnier et al. 2007; Figs. 12(a and b)]. A boundary condition of zero hydraulic head was assigned to the top surface of the foundation located on the landside, since no impounding of the water was allowed during the test and to simulate a water outlet zone. The downstream slope face of the embankment was kept free to drain the groundwater flow. A summary of the analysis phases, along with a concise description of each calculation procedure used, is presented in Table 4.

Results of the Numerical Simulations

To validate the soil characterization adopted in the FE simulations associated to centrifuge Test 1, a comparison between experimental data recorded from all the tensiometers embedded in the embankment body and the corresponding stress points in the numerical simulations is reported in Figs. 13(a and b). The trends of PWPs measured by tensiometers located at the base of the embankment (2-3-5-6) are separated from those recorded by the instruments placed at lower depth (7-8-9-10).

A good agreement can be observed from this comparison, globally confirming the validity of the scaling laws adopted on model geometry, time, and soil parameters carried out so far. More specifically, pore pressures measured at tensiometers 2-6-7-8-9 are very similar to those calculated by FE modeling. On the contrary, experimental data series from tensiometers 3 and 5, at the bottom of the embankment, seem to be quite flat, while the numerical results appear much more sensitive to the external hydraulic loading. It can be presumed that these sensors have not provided representative data for the hydraulic response of the filling material, being installed close to the interface with the foundation layer and eventually including in their monitoring area a certain volume of fine-grained material. The trend of the suction calculated in correspondence of tensiometer 3 slightly deviates from that recorded during the centrifuge test. Fig. 14 summarizes the results of the transient seepage analysis associated to centrifuge Test 1, in terms of PWP contours, incremental deviatoric plastic strains, $\Delta\gamma_s$, and failure plastic points, with reference to three significant time steps: (1) at the beginning

Table 3. Physical and mechanical properties of the embankment and foundation units, according to HS and MCC constitutive models

Soil	Model	γ_{dry} (kN/m^3)	γ_{sat} (kN/m^3)	e_{init*}	E_{50}^{ref} (kN/m^2)	E_{oed}^{ref} (kN/m^2)	E_{ur}^{ref} (kN/m^2)	c' (kN/m^2)	φ' (degrees)	ν	λ	κ	M
TS70-PON30	HS	20.8	22.3	0.31	22.5×10^3	10.0×10^3	67.6×10^3	3.00	46.00	0.223	—	—	—
PON	MCC	17.51	21.01	0.55	—	—	—	—	—	0.20	0.074	0.055	1.33

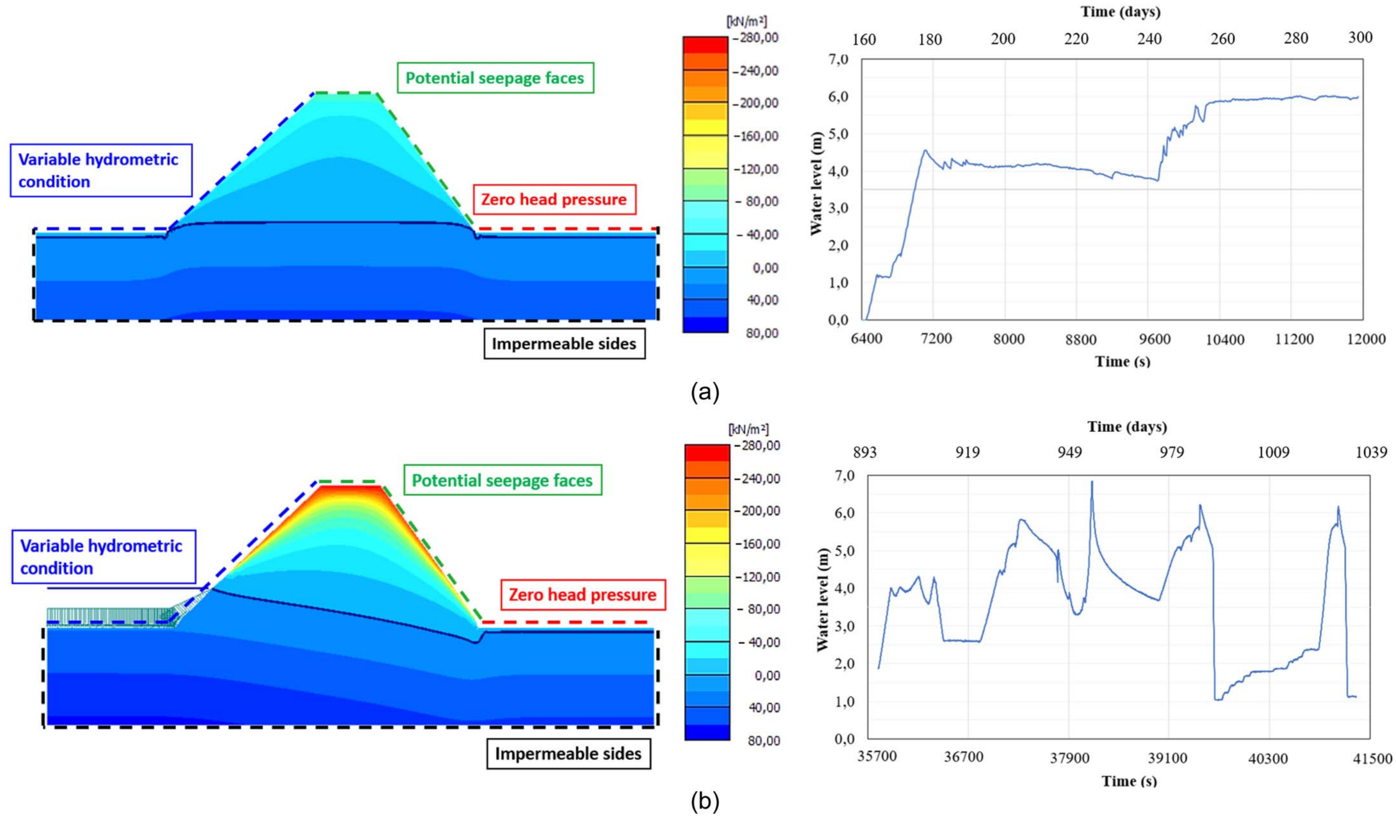

Fig. 12. Initial and boundary conditions assumed at the beginning of the flooding stage (calculation phase 4) for: (a) Test 1; and (b) Test 2. Numerical models on the left, time histories of loading on the right. Time is indicated at the model and prototype scale. The blue bold line indicates the estimated position of the phreatic surface before the application of water level variation. Contour maps show PWP and suction ranges.

Table 4. Stages of the numerical FE modeling analyses

Stages of the analysis	Calculation type	Description
1. Initial stress generation for the foundation layer	K0-procedure	*K0 procedure is a calculation method used to define the initial stresses for the model, taking into account the loading history of the soil, including the preconsolidation stress.*
2. Construction of the embankment	Plastic analysis	*A plastic calculation is used to carry out an elastic-plastic deformation analysis. It includes a steady-state water pressure calculation based on the input of water conditions and pore water pressure distribution imposed.*
3. Self-weight equilibrium 4. Variation of the imposed boundary hydraulic conditions (flooding stage)	Fully coupled flow–deformation analysis Fully coupled flow–deformation analysis	*A fully coupled flow–deformation analysis is conducted when it is necessary to analyze the simultaneous development of deformations and pore pressures in saturated and partially saturated soils, as a result of time dependent changes of the hydraulic boundary conditions.*

of the first hydrometric peak ($t_2 = 190$ days), (2) at the beginning of the second hydrometric peak ($t_3 = 260$ days), and (3) at the end of the second hydrometric peak ($t_3 = 295$ days).

At the beginning of the first hydrometric peak [Fig. 14(a)], about one-third of the embankment turns out to be in saturated conditions; this outcome can be fairly attributable to the retention properties and to the hydraulic conductivity that characterize the TS70-PON30 mixture. As a result of the water level increment, excess PWPs develop in the foundation layer. When the maximum river level is attained, a significant increase in the PWP in the entire riverbank section suddenly occurs [Fig. 14(b)]. The persistence of the second hydrometric peak causes the advancement of the saturation line within the embankment body up to involve an area adjacent to the crest of the embankment [Fig. 14(c)]. The saturation of the embankment is accompanied by an increase in the PWP, which results in a reduction in the soil shear strength and in the generation of deviatoric strains and plastic failure points, whose values and number tend to slight increase, as the hydrometric level

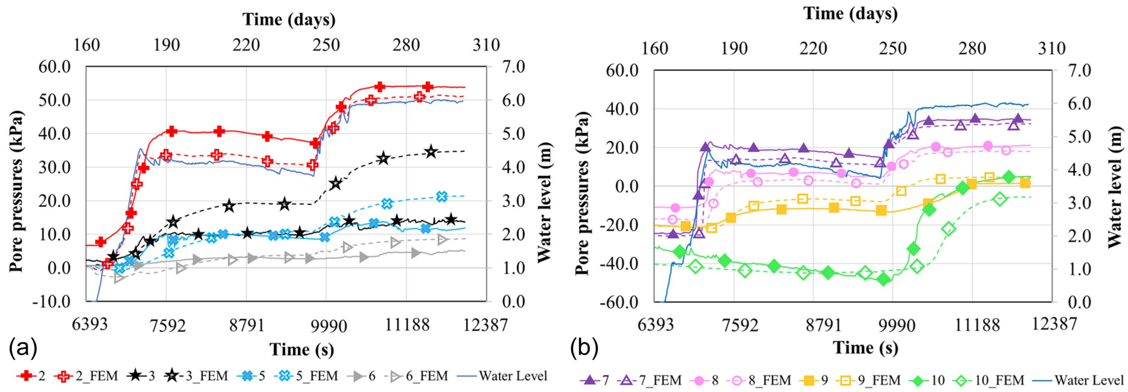

Fig. 13. Test 1, comparison between experimental and numerical results during the flooding stage of the analysis: PWPs recorded in the embankment by tensiometers: (a) 2-3-5-6; and (b) 7-8-9-10.

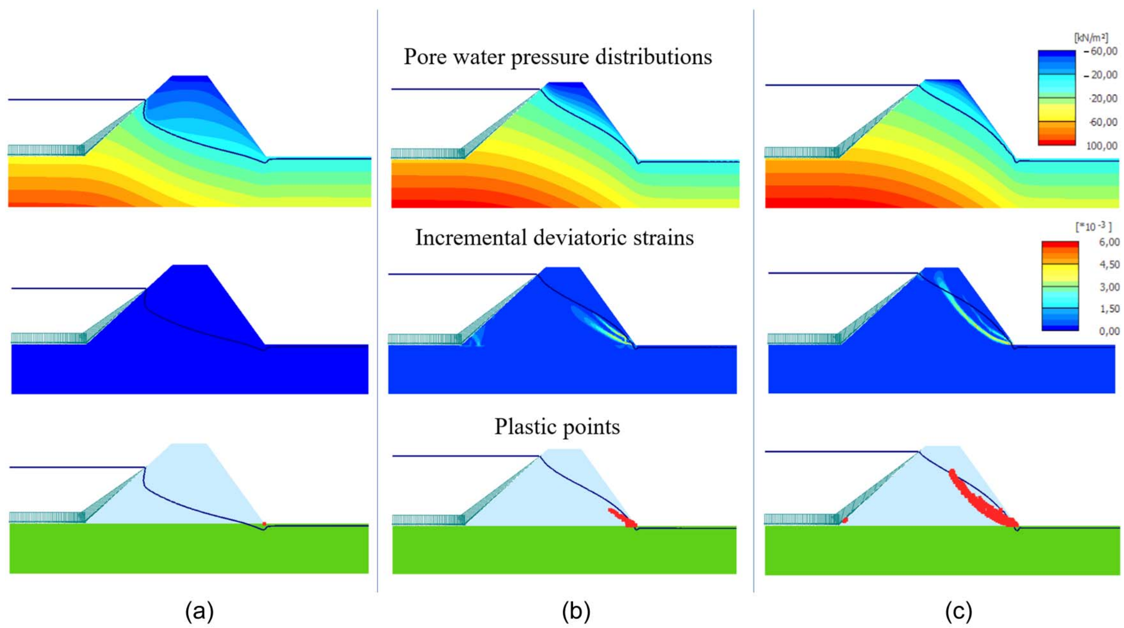

Fig. 14. Results of the numerical simulations associated to centrifuge Test 1—PWPs distributions, incremental deviatoric strains, and plastic points at three significant time steps: (a) at the beginning of the first hydrometric peak (H = 4.3 m; $t_2 = 190$ days); (b) at the beginning of the second hydrometric peak (H = 5.98 m; $t_3 = 260$ days); and (c) at the end of the second hydrometric peak (H = 5.98 m; $t_4 = 295$ days). Isoline increment equal to 10 kPa, plastic points are represented by circles.

approaches its maximum, suggesting a weakening of the landside toe, although not leading to a failure mechanism. Nevertheless, the safety analysis carried out by using the *phi-c* reduction method (Bentley Systems Incorporated 2020) implemented in the software showed that the Factor of Safety associated to the last step of the seepage process is 1.12, indicating a stable configuration of the earth structure, even when the steady-state condition is attained.

To quantify the accuracy of the numerical prediction with respect to the experimental benchmark, the results of the FE simulations, in terms of PWPs at significant time steps, have been plotted against the corresponding physical model tensiometer recordings in Fig. 15, highlighting the scatter of ±10% and 25%, with respect to the line at 45° degrees, representing the perfect coincidence among data. Only four tensiometers have been considered for comparative analysis, being representative of the three different depths instrumented (2, 7, 10) and of the core of the embankment (8).

The time steps selected for the comparison corresponds to (1) the beginning of the first water level increment ($t = 190$ days), (2) the end of the first hydrometric peak persistence ($t = 260$ days); and (3) the end of the second hydrometric peak persistence ($t = 295$ days). A very good agreement between measured and computed data recorded is observed for the time steps considered, with a scatter that never exceeds the ±10% lines. Only at $t = 295$ days does the simulated response of tensiometer 8 not fall within the ±25% scatter lines.

The numerical tool validated against the experimental benchmark was used to reproduce the hydromechanical behavior of the river embankment model subjected to a sequence of hydrometric peaks and drawdowns, simulated during centrifuge Test 2. The results of the fully coupled numerical analyses in terms of PWP trends versus time recorded by the eight tensiometers installed in the embankment body are compared to the results of the centrifuge test in Figs. 16(a and b), in the time interval corresponding to the

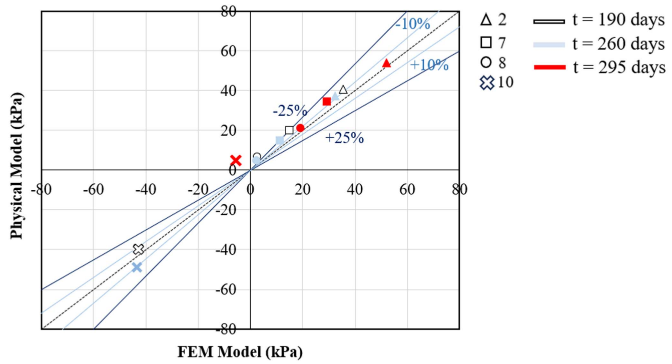

Fig. 15. PWP recorded by tensiometers 2, 7, 8 and 10 at $t = 190$; 260; 295 days ($t = 7{,}276$; 10,389; 11,787 s at the model scale).

flooding stage, showing a good overlapping. Tensiometers 6 and 10 have not been represented, as they ceased to work during the in-flight consolidation stage. Tensiometer 9 shows a peak of PWP, related to the instantaneous overtopping, which occurred at $t =$ 955 days (prototype scale), and has not been numerically detected.

Application to a Real Case Study and Concluding Remarks

In order to evaluate the impact of different hydraulic properties on the safety conditions of the river embankment, a real hydrograph, remodulated proportionally to the height of the model embankment, has been selected and imposed as boundary condition to the riverside of the numerical model previously presented and calibrated. The hydraulic loading history was taken from the water level measured by the Fossalta (MO, Northern Italy) hydrometric station, shown in Fig. 17, during the high-water event that on December 6, 2020, caused a breach in a river embankment located in Castelfranco Emilia, 8 km to the south. Figs. 17(a–c) shows the location of the Fossalta station, a picture of the breach that occurred in Castelfranco Emilia, and the water level imposed in the numerical analysis, respectively. A LiDAR survey conducted before the breach showed that the failed embankment was 5 m high, 16 m wide at the base, the crest width was within 2 and 3.5 m, and the slope inclination angle was between 35° and 50° (Ceccato and Simonini 2023). Geotechnical investigations carried out after the collapse in the area of the breach evidenced that the embankment was made of a sand–silt mixture in different proportions, while the foundation was made of sandy silt and silty sand up to 15 m depth. Incidentally, reasons for the collapse were identified in the increase in PWP, combined with preexisting heterogeneities and small cavities in the embankment, which contributed to the triggering of a local failure on the landside slope and of a subsequent internal erosion process that eventually led to a global failure (Menduni et al. 2021; Ceccato and Simonini 2023). The Fossalta section, where the water level was recorded, remained consistently stable.

The results of the transient coupled flow–deformation analysis carried out with the software PLAXIS 2D, in terms of PWP distributions over time, are reported in Fig. 18, in correspondence of the most significant time steps. The hydraulic conditions measured at the end of the consolidation stage of the centrifuge Test 1 were assumed as initial conditions [Fig. 18(a)]. It can be noted that the short persistence of the first hydrometric peak [Fig. 18(b)] is not sufficient to saturate the embankment core and the phreatic surface remain close to the riverside. This is also due to the initial suction distribution within the embankment, which of course contributes to the initially low soil permeability. The sequence of hydrometric peaks, despite having a lower height, leads to a slight yet gradual rise in PWPs within the foundation layer, both along the riverside and beneath the footprint of the embankment, the embankment core persisting unsaturated though.

During the rapid drawdown phenomena, which occurred after each hydrometric peak, the soil close to the river remains in saturated conditions, due to the retention properties of the silty sand, potentially leading to the subsequent failure of the riverside slope. As far as the stability of the embankment is concerned, the *phi-c* reduction method provided a Factor of Safety equal to 1.710 under the most unfavorable scenario (i.e., during the occurrence of the first hydrometric peak). Despite that soil parameters used in the numerical analyses referred to the materials tested in the centrifuge, results clearly show that reaching saturation inside such embankments is unlikely under realistic critical hydrographs and that possible failures are often rather the consequence of internal erosion triggered by local heterogeneities or instabilities, not reproduced by these numerical analyses. However, they are essential to achieve a reliable assessment of the actual safety conditions under transient flow and variable hydraulic conditions.

As proof of concept, in compliance with the semiprobabilistic approach prescribed by Eurocode 7 (CEN 2004) and adopted in common engineering practice, an additional numerical simulation has been carried out by assigning to the embankment and foundation units only saturated parameters and by imposing a steady-state

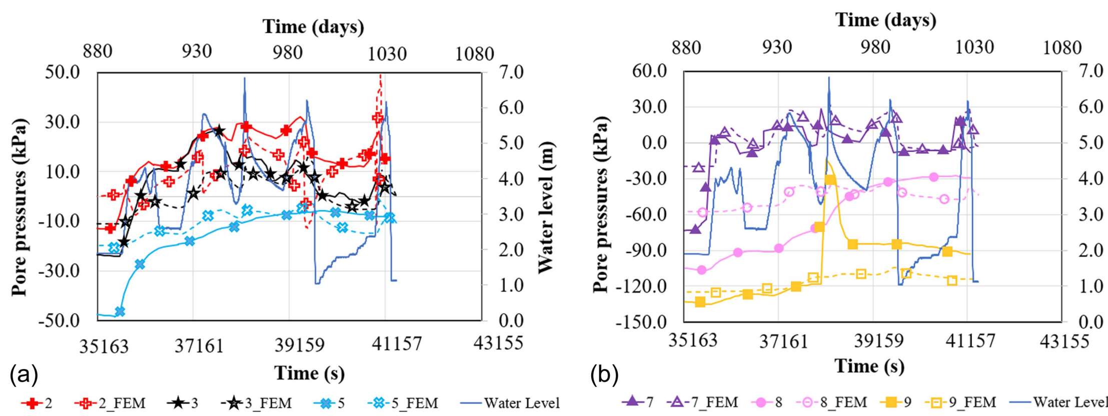

Fig. 16. Test 2, comparison between experimental and numerical results during the flooding stage of the analysis: PWP recorded in the embankment by tensiometers: (a) 2-3-5; and (b) 7-8-9.

Fig. 17. (a) Location of the monitoring station in Fossalta (base map © Esri, USGS | Esri (2025), TomTom, Garmin, FAO, NOAA, USGS | Earthstar Geographics); (b) picture of the breach that occurred in Castelfranco Emilia (Italy) on December 6, 2020 [reprinted from Ceccato and Simonini 2023, under Creative Commons 4.0 Deed (https://creativecommons.org/licenses/by/4.0/deed.en)]; and (c) comparison between the measured hydrograph and the water level remodulated and imposed in the numerical analysis.

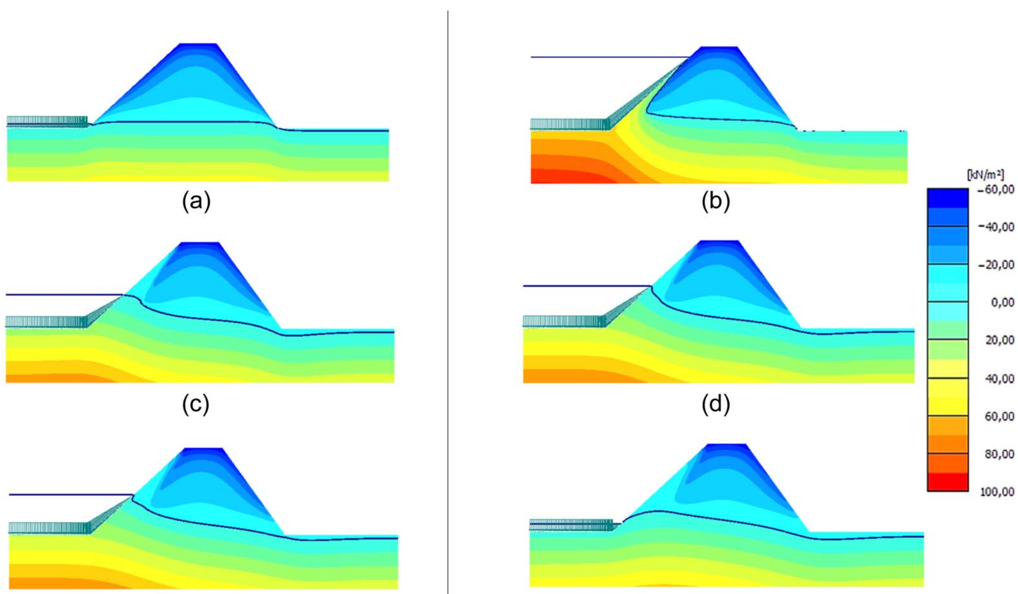

Fig. 18. Contours of PWP distributions at significant time steps: (a) initial conditions; (b) first hydrometric peak; (c) first drawdown; (d) second hydrometric peak; (e) third hydrometric peak; and (f) third drawdown. Isoline increment is equal to 10 kPa.

flow regime, in equilibrium with the maximum water level of the remodulated hydrograph (6.02 m). Results in terms of PWP distributions and stability conditions are reported in Figs. 19(a and b), showing that the phreatic surface reaches a considerable height on the landside slope (half of the overall embankment elevation), and the hydraulic conductivity of the embankment material—neglecting its variability associated to suction—strongly affects the water capacity infiltration and the global Factor of Safety of the river embankment results equal to 0.891. A possible critical slip surface is highlighted in Fig. 19(b), through the incremental deviatoric strain contours. The comparison between Figs. 14(c) and 19 highlights that a proper modeling of the unsaturated soil and of the corresponding effective stress field above the saturation line results in a significant enhancement of the related soil shear strength, with respect to modeling the embankment as saturated, with a hydrostatic distribution of pore pressure above the phreatic line increasing the factor of safety from 0.891 to 1.12. It can therefore be concluded that (1) the simplified assumption of a steady-state seepage inside the river embankment could often result excessively conservative, because such regime is typically attained only after an unrealistic persistence of the hydrometric peak; and (2) if the steady-state conditions are attained (i.e., everything else being equal), modeling the embankment soil as partially saturated above the phreatic line is decisive.

The extensive laboratory investigation and the centrifuge tests carried out and herein described, together with a predictive numerical

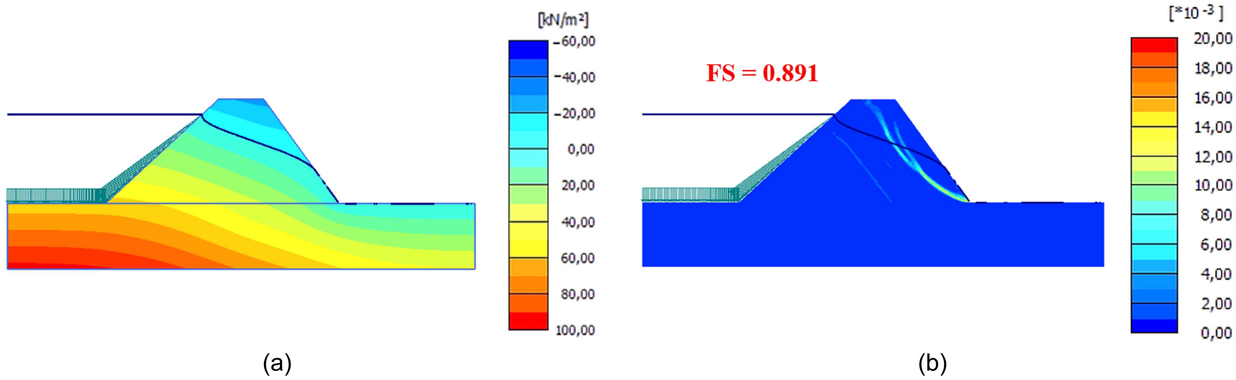

Fig. 19. Results of the seepage and stability analyses, in terms of: (a) PWP contours; and (b) incremental deviatoric strains, together with the Factor of Safety toward failure mechanisms.

tool entirely calibrated on the basis of the experimental results, enable a careful and realistic assessment of the hydromechanical response of full-scale river embankments, proving that the proposed integrated approach represents a significant advancement for the design of such critical earth infrastructures, both existing and of new construction.

Data Availability Statement

Laboratory data and the results obtained from FE numerical analyses, all supporting the findings of the present study, are owned by the authors and can be made available from the corresponding author upon reasonable request.

Acknowledgments

The study is part of the "RedReef project," an acronym of "Risk Assessment of Earth Dams and River Embankments to Earthquakes and Floods" (Grant Agreement 2017YPMBWJ), funded by the Italian Ministry of University and Research.

References

Airoldi, S., V. Fioravante, and D. Giretti. 2016. "The ISMGEO geotechnical centrifuge." In *Proc., EUROFUGE 2016—Nantes*, edited by Thorel, Bretschneider, Blanc and Escoffier. Nantes, France: IFSTTAR.

Amabile, A., A. Pozzato, and A. Tarantino. 2020. "Instability of flood embankments due to pore-water pressure build-up at the toe: Lesson learned from the Adige River case study." *Can. Geotech. J.* 57 (12): 1844–1853. https://doi.org/10.1139/cgj-2018-0372.

ASTM. 2020. *Test method for consolidated drained triaxial compression test for soils*. ASTM D7181-20(2020). West Conshohocken, PA: ASTM.

ASTM. 2021. *Test methods for laboratory compaction characteristics of soil using standard effort (12,400 ft-lbf/ft3 (600 kN-m/m3))*. ASTM D698-12(2021). West Conshohocken, PA: ASTM.

Baldi, G., G. Belloni, and W. Maggioni. 1988. *The ISMES geotechnical centrifuge*. Rotterdam, Netherlands: A.A. Balkema.

Bentley Systems Incorporated. 2020. *PLAXIS 2D-reference manual*. Delft, Netherlands: Bentley Systems Incorporated.

Bishop, A. W. 1959. "The principle of effective stress." *Tek. Ukebl.* 106 (39): 859–863.

Blatz, J. A., W. A. Take, and D. Priyanto. 2006. "Influence of a weathered zone on the susceptibility of a slope to rainfall induced instability." In *Unsaturated soils 2006*, 2291–2299. Reston, VA: ASCE.

Caicedo, B., and L. Thorel. 2014. "Principles of physical modelling of unsaturated soils." In *Proc., 8th Int. Conf. on Physical Modelling in Geotechnics 2014 (ICPMG2014): ICPMG2014—Physical Modelling in Geotechnics*, edited by C. Gaudin and D. White, 77–98. Boca Raton, FL: CRC Press.

Calabresi, G., F. Colleselli, D. Danese, G. Giani, C. Mancuso, L. Montrasio, A. Nocilla, L. Pagano, E. Reali, and A. Sciotti. 2013. "Research study of the hydraulic behaviour of the Po River embankments." *Can. Geotech. J.* 50 (9): 947–960. https://doi.org/10.1139/cgj-2012-0339.

Cargill, K. W., and H. Ko. 1983. "Centrifugal modeling of transient water flow." *J. Geotech. Eng.* 109 (4): 536–555. https://doi.org/10.1061/(ASCE)0733-9410(1983)109:4(536).

Ceccato, F., and P. Simonini. 2023. "The effect of heterogeneities and small cavities on levee failures: The case study of the Panaro levee breach (Italy) on 6 December 2020." *J. Flood Risk Manage.* 16 (2): e12882. https://doi.org/10.1111/jfr3.12882.

CEN (European Committee for Standardization). 2004. *Eurocode 7: Geotechnical design—Part 1: General rules*. EN 1997-1. Brussels, Belgium: CEN.

CEN ISO/TS 17892-11:2004 - UNI Ente Italiano di Normazione. 2004. Geotechnical investigation and testing—Laboratory testing of soil—Part 11: Determination of permeability by constant and falling head." Accessed December 28, 2023. https://store.uni.com/cen-iso-ts-17892-11-2004.

Chen, C., and L. Zhang. 2023. "Hydro-mechanical behaviour of soil experiencing seepage erosion under cyclic hydraulic gradient." *Géotechnique* 73 (2): 115–127. https://doi.org/10.1680/jgeot.20.P.340.

Clarke, D., and J. A. Smethurst. 2010. "Effects of climate change on cycles of wetting and drying in engineered clay slopes in England." *Q. J. Eng. Geol. Hydrogeol.* 43 (4): 473–486. https://doi.org/10.1144/1470-9236/08-106.

Darcy, H. 1856. *Les Fontaines Publiques de la Ville de Dijon: Exposition et Application des Principes a Suivre et des Formulesa Employer dans les Questions de Distribution d'Eau*. Paris: Dalmont, V.

Dias, A. S., M. Pirone, M. V. Nicotera, and G. Urciuoli. 2022. "Hydraulic hysteresis of natural pyroclastic soils in partially saturated conditions: Experimental investigation and modeling." *Acta Geotech.* 17 (3): 837–855. https://doi.org/10.1007/s11440-021-01273-y.

Duncan, J. M., and C.-Y. Chang. 1970. "Nonlinear analysis of stress and strain in soils." *J. Soil Mech. Found. Div.* 96 (5): 1629–1653. https://doi.org/10.1061/JSFEAQ.0001458.

Esri. 2025. "World imagery." *ArcGIS Online.* Accessed January 21, 2025. https://server.arcgisonline.com/arcgis/rest/services/World_Imagery/MapServer.

Farias, M. M. D., and M. P. Cordão Neto. 2010. "Advanced numerical simulation of collapsible earth dams." *Can. Geotech. J.* 47 (12): 1351–1364. https://doi.org/10.1139/T10-032.

Fioravante, V. 2000. "Anisotropy of small strain stiffness of Ticino and Kenya sands from seismic wave propagation measured in triaxial testing." *Soils Found.* 40 (4): 129–142. https://doi.org/10.3208/sandf.40.4_129.

Fioravante, V., and D. Giretti. 2016. "Unidirectional cyclic resistance of Ticino and Toyoura sands from centrifuge cone penetration tests." *Acta Geotech.* 11 (4): 953–968. https://doi.org/10.1007/s11440-015-0419-3.

Fredlund, D. G., and H. Rahardjo. 1993. *Soil mechanics for unsaturated soils*. Hoboken, NJ: Wiley.

Garnier, J., C. Gaudin, S. M. Springman, P. J. Culligan, D. Goodings, D. Konig, B. Kutter, R. Phillips, M. F. Randolph, and L. Thorel. 2007. "Catalogue of scaling laws and similitude questions in geotechnical centrifuge modeling." *Int. J. Phys. Modell. Geotech.* 7 (3): 1–23. https://doi.org/10.1680/ijpmg.2007.070301.

Gottardi, G., C. G. Gragnano, M. Ranalli, and L. Tonni. 2020. "Reliability analysis of riverbank stability accounting for the intrinsic variability of unsaturated soil parameters." *Struct. Saf.* 86 (Sep): 101973. https://doi.org/10.1016/j.strusafe.2020.101973.

Gottardi, G., C. G. Gragnano, I. Rocchi, and M. Bittelli. 2016. "Assessing river embankment stability under transient seepage conditions." *Procedia Eng.* 158 (Jan): 350–355. https://doi.org/10.1016/j.proeng.2016.08.454.

Gragnano, C. G., I. Rocchi, and G. Gottardi. 2021. "Field monitoring and laboratory testing for an integrated modeling of river embankments under transient conditions." *J. Geotech. Geoenviron. Eng.* 147 (9): 05021006. https://doi.org/10.1061/(ASCE)GT.1943-5606.0002571.

Harvard, B. R., and A. T. Corey. 1964. "Hydraulic properties of porous media and their relation to drainage design." *Trans. ASAE* 7 (1): 26–28. https://doi.org/10.13031/2013.40684.

Higo, Y., C.-W. Lee, T. Doi, T. Kinugawa, M. Kimura, S. Kimoto, and F. Oka. 2015. "Study of dynamic stability of unsaturated embankments with different water contents by centrifugal model tests." *Soils Found.* 55 (1): 112–126. https://doi.org/10.1016/j.sandf.2014.12.009.

Hird, C. C., A. Marsland, and A. N. Schofield. 1978. "The development of centrifugal models to study the influence of uplift pressures on the stability of a flood bank." *Géotechnique* 28 (1): 85–106. https://doi.org/10.1680/geot.1978.28.1.85.

Hueckel, T., and G. Baldi. 1990. "Thermoplasticity of saturated clays: Experimental constitutive study." *J. Geotech. Eng.* 116 (12): 1778–1796. https://doi.org/10.1061/(ASCE)0733-9410(1990)116:12(1778).

Hueckel, T. A. 1992. "Water–mineral interaction in hygromechanics of clays exposed to environmental loads: A mixture-theory approach." *Can. Geotech. J.* 29 (6): 1071–1086. https://doi.org/10.1139/t92-124.

Jafari, N. H., J. A. Cadigan, T. D. Stark, and M. L. Woodward. 2019. "Phreatic surface migration through an unsaturated levee embankment." *J. Geotech. Geoenviron. Eng.* 145 (11): 05019010. https://doi.org/10.1061/(ASCE)GT.1943-5606.0002139.

Kirste, B., S. C. Iden, and W. Durner. 2019. "Determination of the soil water retention curve around the wilting point: Optimized protocol for the dewpoint method." *Soil Sci. Soc. Am. J.* 83 (2): 288–299. https://doi.org/10.2136/sssaj2018.08.0286.

Lu, N., and W. J. Likos. 2004. *Unsaturated soil mechanics*. Research Rep. No. 86–6. Hoboken, NJ: Wiley.

Menduni, G., R. Cocchi, L. Manselli, and P. Simonini. 2021. *Relazione di dettaglio*. Modena, Italy: Commissione tecnico-scientifica per la valutazione delle cause all'origine della rotta arginale lungo il fiume Panaro in località Gaggio di Castelfranco Emilia, Regione Emilia-Romagna, Modena.

Mitchell, R. J. 1994. "Centrifuge techniques for testing clay liner samples." *Can. Geotech. J.* 31 (4): 577–583. https://doi.org/10.1139/t94-067.

Moffat, R., and R. J. Fannin. 2011. "A hydromechanical relation governing internal stability of cohesionless soil." *Can. Geotech. J.* 48 (3): 413–424. https://doi.org/10.1139/T10-070.

Mualem, Y. 1976. "A new model for predicting the hydraulic conductivity of unsaturated porous media." *Water Resour. Res.* 12 (3): 513–522. https://doi.org/10.1029/WR012i003p00513.

Muir Wood, D., and J. Graham. 1990. "Anisotropic elasticity and yielding of a natural plastic clay." *Int. J. Plast.* 6 (4): 377–388. https://doi.org/10.1016/0749-6419(90)90009-4.

Orlandini, S., G. Moretti, and J. D. Albertson. 2015. "Evidence of an emerging levee failure mechanism causing disastrous floods in Italy." *Water Resour. Res.* 51 (10): 7995–8011. https://doi.org/10.1002/2015WR017426.

Padfield, C. J. 1979. *Stability of river banks and flood embankments: A centrifugal model study of the influence of the interaction of two deforming layers in the analysis of river bank stability problems*. Cambridge, UK: Apollo–Univ. of Cambridge Repository.

Padfield, C. J., and A. N. Schofield. 1983. "The development of centrifugal models to study the influence of uplift pressures on the stability of a flood bank." *Géotechnique* 33 (1): 57–66. https://doi.org/10.1680/geot.1983.33.1.57.

Palladino, M. R., S. Barbetta, S. Camici, P. Claps, and T. Moramarco. 2020. "Impact of animal burrows on earthen levee body vulnerability to seepage." *J. Flood Risk Manage.* 13 (S1): e12559. https://doi.org/10.1111/jfr3.12559.

Pertassek, T., A. Peters, and W. Durner. 2015. *HYPROP-FIT Software User's Manual, V.3.0, UMS GmbH*. München, Germany: UMS GmbH.

Peters, A., and W. Durner. 2008. "A simple model for describing hydraulic conductivity in unsaturated porous media accounting for film and capillary flow." *Water Resour. Res.* 44 (11). https://doi.org/10.1029/2008WR007136.

Rinaldi, M., N. Casagli, S. Dapporto, and A. Gargini. 2004. "Monitoring and modelling of pore water pressure changes and riverbank stability during flow events." *Earth Surface Process. Landforms Sediment Deposits* 29 (2): 237–254. https://doi.org/10.1002/esp.1042.

Rivera-Hernandez, X. A., G. S. Ellithy, and F. Vahedifard. 2019. "Integrating field monitoring and numerical modeling to evaluate performance of a levee under climatic and tidal variations." *J. Geotech. Geoenviron. Eng.* 145 (10): 05019009. https://doi.org/10.1061/(ASCE)GT.1943-5606.0002134.

Rotisciani, G. M., L. M. Lalicata, A. Desideri, and F. Casini. 2020. "Numerical modelling of the response of an unsaturated silty soil under wetting and gravitational loading processes." In Vol. 195 of *Proc., E3S Web of Conf.*, edited by R. Cardoso, C. Jommi, and E. Romero, 02012. Les Ulis, France: EDP Sciences. https://doi.org/10.1051/e3sconf/202019502012.

Saghaee, G., A. A. Mousa, and M. A. Meguid. 2017. "Plausible failure mechanisms of wildlife-damaged earth levees: Insights from centrifuge modeling and numerical analysis." *Can. Geotech. J.* 54 (10): 1496–1508. https://doi.org/10.1139/cgj-2016-0484.

Saran, R. K., and B. V. S. Viswanadham. 2018. "Centrifuge model tests on the use of geosynthetic layer as an internal drain in levees." *Geotext. Geomembr.* 46 (3): 257–276. https://doi.org/10.1016/j.geotexmem.2017.12.004.

Schindler, U., W. Durner, G. Von Unold, L. Mueller, and R. Wieland. 2010. "The evaporation method: Extending the measurement range of soil hydraulic properties using the air-entry pressure of the ceramic cup." *J. Plant Nutr. Soil Sci.* 173 (4): 563–572. https://doi.org/10.1002/jpln.200900201.

Schindler, U., and L. Müller. 2017. "Soil hydraulic functions of international soils measured with the Extended Evaporation Method (EEM) and the HYPROP device." *Open Data J. Agric. Res.* 3 (May): 10–16. https://doi.org/10.18174/odjar.v3i1.15763.

Singh, D. N., and A. K. Gupta. 2000. "Modelling hydraulic conductivity in a small centrifuge." *Can. Geotech. J.* 37 (5): 1150–1155. https://doi.org/10.1139/t00-027.

Singh, D. N., and S. J. Kuriyan. 2002. "Estimation of hydraulic conductivity of unsaturated soils using a geotechnical centrifuge." *Can. Geotech. J.* 39 (3): 684–694. https://doi.org/10.1139/t02-013.

Singh, J., K. Horikoshi, Y. Mochida, and A. Takahashi. 2019. "Centrifugal tests on minimization of flood-induced deformation of levees by steel drainage pipes." *Soils Found.* 59 (2): 367–379. https://doi.org/10.1016/j.sandf.2018.12.008.

Stirling, R. A., D. G. Toll, S. Glendinning, P. R. Helm, A. Yildiz, P. N. Hughes, and J. D. Asquith. 2021. "Weather-driven deterioration processes affecting the performance of embankment slopes." *Géotechnique* 71 (11): 957–969. https://doi.org/10.1680/jgeot.19.SiP.038.

Theriault, J. A., and R. J. Mitchell. 1997. "Use of a modelling centrifuge for testing clay liner compatibility with permeants." *Can. Geotech. J.* 34 (1): 71–77. https://doi.org/10.1139/t96-102.

Van, M. A., A. R. Koelewijn, and F. B. Barends. 2005. "Uplift phenomenon: Model, validation, and design." *Int. J. Geomech.* 5 (2): 98–106. https://doi.org/10.1061/(ASCE)1532-3641(2005)5:2(98).

Van Genuchten, M. T. 1980. “A closed-form equation for predicting the hydraulic conductivity of unsaturated soils.” *Soil Sci. Soc. Am. J.* 44 (5): 892–898. https://doi.org/10.2136/sssaj1980.03615995004400050002x.

Ventini, R., E. Dodaro, D. Giretti, M. Pirone, F. Zarattini, C. G. Gragnano, V. Fioravante, F. Gabrieli, G. Gottardi, and C. Mancuso. 2023. “Analysis of transient seepage through a river embankment by means of centrifuge modelling.” In *Proc., 8th Int. Conf. on Unsaturated Soils–UNSAT 23*, edited by M. Bardanis. Les Ulis, France: EDP Sciences. https://doi.org/10.1051/e3sconf/202338212008.

Ventini, R., E. Dodaro, C. G. Gragnano, D. Giretti, and M. Pirone. 2021. “Experimental and numerical investigations of a river embankment model under transient seepage conditions.” *Geosciences* 11 (5): 192. https://doi.org/10.3390/geosciences11050192.

Vorster, P., P. Gräbe, and S. Jacobsz. 2017. “Centrifuge modelling of railway embankments under static and cyclic loading.” *J. South African Inst. Civ. Eng.* 59 (3): 2–10. https://doi.org/10.17159/2309-8775/2017/v59n3a1.

Wang, Z., J. Feyen, D. R. Nielsen, and M. T. Van Genuchten. 1997. “Two-phase flow infiltration equations accounting for air entrapment effects.” *Water Resour. Res.* 33 (12): 2759–2767. https://doi.org/10.1029/97WR01708.

Zhang, Y., A. Zhou, M. Nazem, and J. Carter. 2019. “Finite element implementation of a fully coupled hydro-mechanical model and unsaturated soil analysis under hydraulic and mechanical loads.” *Comput. Geotech.* 110 (Jan): 222–241. https://doi.org/10.1016/j.compgeo.2019.02.005.

J. Geotech. Geoenviron. Eng., 2025, 151(8): 04025075